



Multi-objective optimization and evaluation of supercritical CO₂ Brayton cycle for nuclear power generation

Guo-Peng Yu¹ · Yong-Feng Cheng² · Na Zhang² · Ping-Jian Ming¹

Received: 9 June 2023 / Revised: 13 July 2023 / Accepted: 25 August 2023 / Published online: 5 February 2024

© The Author(s), under exclusive licence to China Science Publishing & Media Ltd. (Science Press), Shanghai Institute of Applied Physics, the Chinese Academy of Sciences, Chinese Nuclear Society 2024

Abstract

The supercritical CO₂ Brayton cycle is considered a promising energy conversion system for Generation IV reactors for its simple layout, compact structure, and high cycle efficiency. Mathematical models of four Brayton cycle layouts are developed in this study for different reactors to reduce the cost and increase the thermohydraulic performance of nuclear power generation to promote the commercialization of nuclear energy. Parametric analysis, multi-objective optimizations, and four decision-making methods are applied to obtain each Brayton scheme's optimal thermohydraulic and economic indexes. Results show that for the same design thermal power scale of reactors, the higher the core's exit temperature, the better the Brayton cycle's thermo-economic performance. Among the four-cycle layouts, the recompression cycle (RC) has the best overall performance, followed by the simple recuperation cycle (SR) and the intercooling cycle (IC), and the worst is the reheating cycle (RH). However, RH has the lowest total cost of investment (C_{tot}) of \$1619.85 million, and IC has the lowest levelized cost of energy (LCOE) of 0.012 \$(/kWh). The nuclear Brayton cycle system's overall performance has been improved due to optimization. The performance of the molten salt reactor combined with the intercooling cycle (MSR-IC) scheme has the greatest improvement, with the net output power (W_{net}), thermal efficiency η_t , and exergy efficiency (η_e) improved by 8.58%, 8.58%, and 11.21%, respectively. The performance of the lead-cooled fast reactor combined with the simple recuperation cycle scheme was optimized to increase C_{tot} by 27.78%. In comparison, the internal rate of return (IRR) increased by only 7.8%, which is not friendly to investors with limited funds. For the nuclear Brayton cycle, the molten salt reactor combined with the recompression cycle scheme should receive priority, and the gas-cooled fast reactor combined with the reheating cycle scheme should be considered carefully.

Keywords Supercritical CO₂ Brayton cycle · Nuclear power generation · Thermo-economic analysis · Multi-objective optimization · Decision-making methods

Guo-Peng Yu and Yong-Feng Cheng have contributed equally to this work.

This work was supported of National Natural Science Foundation of China Fund (No. 52306033), State Key Laboratory of Engines Fund (No. SKLE-K2022-07), and the Jiangxi Provincial Postgraduate Innovation Special Fund (No. YC2022-s513).

✉ Guo-Peng Yu
yugp3@mail.sysu.edu.cn

✉ Ping-Jian Ming
mingpj@mail.sysu.edu.cn

¹ Sino-French Institute of Nuclear Engineering and Technology, Sun Yat-Sen University, Zhuhai 519082, China

² School of Civil Engineering and Architecture, East China Jiaotong University, Nanchang 330013, China

Abbreviations

GFR	Gas-cooled fast reactor
SFR	Sodium-cooled fast reactor
LFR	Lead-cooled fast reactor
MSR	Molten salt reactor
SR	Simple recuperation cycle
RC	Recompression cycle
RH	Re-heating cycle
IC	Intercooling cycle
SC	Specific cost
LCOE	Levelized cost of energy
IRR	Internal rate of return
PBP	Payback period
SP	Size parameters
APR	Area per net output power
HX	Heat exchanger
HTR	High-temperature recuperator

LTR	Low-temperature recuperator
MC	Main compressor
DMM	Decision-making method
NSGA	Non-dominated sorting genetic algorithm
ORC	Organic Rankine cycle
PC	Pre-cooler
RC	Recompressor
Turb	Turbine
S-CO ₂ BC	Supercritical carbon dioxide Brayton cycle

List of symbols

A	Area, m ²
c	Heat capacity, J/K
C	Cost, \$
CF	Cash flow, \$
d	Flow channel diameter, m
D	Hydraulic diameter, m
f	Friction coefficient
h	Specific enthalpy, kJ/kg
I	Exergy destruction, W
L	Channel length, m
m	Mass flow rate, kg/s
p	Pitch, mm
P	Pressure, kPa
PR	Pressure ratio
Q	Heat energy, W
s	Specific entropy, kJ/(kg K)
t	Thickness, mm
T	Temperature, K
V	Volume flow, m ² /s
W	Work, kJ

Subscripts

0	Ambient conditions
cold	Cold fluid
hot	Hot fluid
e	Exergy
f	Work fluid
net	Net
i	State point
in	Inlet
min	Minimum
max	Maximum
out	Outlet
tot	Total
rev	Revenues
xp	Expenses
c	Compressor
t	Turbine

Greek letters

ε	Surface roughness
η	Efficiency
μ	Kinematic viscosity

δ	Relative roughness
ρ	Density
α	Heat transfer coefficient

1 Introduction

The overuse of fossil energy is one of the major causes of global warming [1]. As one of the most efficient and clean energy sources, nuclear energy has been criticized for its high investment costs [2] and poor safety [3]. However, scholars have not given up their research on nuclear energy, and with the introduction of fourth-generation nuclear reactors, nuclear power generation has gradually become a research hotspot [4–6]. Most current power conversion systems in power plants use the steam Rankine cycle and gas turbine systems. However, the high reactor outlet temperatures and pressures limit the efficiency of nuclear power conversion systems [7]. Compared with the steam Rankine cycle [8], the supercritical carbon dioxide (S-CO₂) power cycle has the advantages of higher system thermal efficiency and a more compact power system equipment structure [9], which makes it well matched with nuclear power applications. However, compared to the advantages of supercritical helium power cycles in ultra-high temperature systems (above 1000 °C), S-CO₂ power cycles are more suitable for medium-temperature operation (450–600 °C) in Generation IV reactors [10]. The advantages of a simple layout and compact structure can save the investment cost of nuclear power generation systems, which is economically more advantageous than other energy types [11]. Simultaneously, the small footprint allows high-power-density nuclear power equipment to be assembled in the factory before being transported to the construction site by truck or train [12], facilitating the commercial use of nuclear power.

Currently, research on the supercritical carbon dioxide Brayton cycle (S-CO₂BC) has focused on system performance optimization [13], working fluid selection [14], techno-economic features, and their combinations with other thermal energy systems [15–17]. Ahn et al. [7] conducted a comparative analysis of S-CO₂BC systems under various cycle layouts and obtained that recompressed Brayton cycle systems have a higher thermal system efficiency and emergency efficiency than other cycle layouts. Kim et al. [18] analyzed the parameters, such as thermal system efficiency and net system output power, as evaluation indices for an S-CO₂ recompressed Brayton cycle system using the pinch-point temperature difference method, optimizing the operating parameters of the system to determine the optimal operating conditions of the heat exchanger and other equipment. Song et al. [19] investigated the combined cycle system of the S-CO₂ Brayton cycle and organic Rankine cycle (ORC), optimizing the system's operating parameters

to improve the thermal performance of the combined cycle system significantly. Bian et al. [20] investigated and compared the effects of different control valves on the dynamic performance of the SCO₂BC system in terms of both thermodynamic and safety performance. Wang et al. [21] investigated the dynamic response characteristics under S-CO₂ Brayton cycle failure conditions and proposed corresponding contingency measures.

All the above studies on the S-CO₂ cycle system use a single objective function for evaluation. Since the single objective function cannot fully reflect the performance characteristics of the S-CO₂ cycle system, many scholars have also established multi-objective functions to research key evaluation parameters of the cycle system, such as thermal efficiency, net output power, and irreversible energy loss of the system. Wang et al. [22] established multi-objective functions, such as system thermal efficiency and net system output power, as evaluation parameters in the application of SCO₂BC in tower solar power systems to optimize various cycle systems, such as the simple recuperation, recompression, and pre-compression cycles. Battisti et al. [23] used the system thermal efficiency and heat transfer coefficient as objective functions in the S-CO₂BC cycle to find the optimal performance of the system based on the variation in the heat source temperature, the mass flow rate of the working fluid on the heat source side, and the maximum temperature of the working fluid, respectively. Nami et al. [24] conducted an exergoeconomic analysis of a cogeneration system, a combined heat and power (CHP) system, including a gas turbine, SCO₂BC, and ORC. The average product unit cost of the system was reduced by 0.56 \$/GJ after optimization, using the sum of investment cost, total endemic damage cost, and environmental impact cost as the objective function. Mohammad et al. [25] optimized the techno-economics of a simple recuperation Brayton cycle based on the genetic algorithm (GA) so that the cycle produces 71% of the maximum power at the optimum point but at a cost rate of only 33% of the maximum power state. Li et al. [26] also considered the ecological performance of the system. They used the non-dominated sorting genetic algorithm (NSGA-II) to optimize the net output power, thermal efficiency, and ecological performance of the Brayton cycle system driven by a hybrid of fossil fuel and solar power.

In multi-objective optimization, due to the conflict between different objectives, optimizing one objective is at the cost of deteriorating other objectives, so obtaining a unique optimal solution is difficult. Instead, coordination and compromise are made among them so that the overall objective is as optimal as possible [27]. The general optimization algorithms all aim to obtain an optimal set of solutions called the Pareto frontier [28]. Many methods have been proposed for obtaining compromise solutions from the Pareto frontier. Li et al. [29] used the NSGA-II method

to optimize the proposed Brayton cycle model. In addition, multi-attribute decision-making methods (MADM), such as TOPSIS, LINMAP, and Shannon entropy, were used to select the optimal system parameters from the Pareto frontier calculated by the NSGA-II method. Arora et al. [30] proposed a thermodynamic model of a simple recuperation Brayton system with irreversibility based on finite-element thermodynamic analysis. The proposed model was optimized using NSGA-II and a multi-objective evolutionary algorithm based on decomposition (MOEAD), and the proposed model was optimized by Shannon entropy, LINMAP, Fuzzy, Bellman–Zadeh, TOPSIS, and other MADM methods to find the optimal system parameters from the Pareto frontier. Rao et al. [31] proposed a new multi-objective optimization method, the Rao algorithm. A combined solar Brayton cycle–power system case study also investigated the proposed Rao algorithm. The MADM method was used to rank the Pareto optimal solutions based on the average rank. Kumar et al. [30] performed a multi-objective optimization of the Brayton cycle system model by NSGA-II, determining the optimal design parameters from the Pareto frontier using MADM methods such as Shannon entropy, LINMAP, Fuzzy, and TOPSIS.

Therefore, most of the research on multi-objective optimization of S-CO₂BC based on nuclear power generation has been limited to thermodynamic performance. In contrast, some research has been conducted on its economics and safety. Also, there are few effective methods for determining the unique optimal solution for multi-objective optimization. This study develops a mathematical model of the Brayton cycle for four different cycle layouts and four Generation IV nuclear reactors. NSGA-II is used to optimize two objectives, η_t and LCOE, simultaneously. The results of the four decision methods are evaluated using Taylor diagrams to obtain the unique optimal solution. Finally, the comprehensive evaluation results of the multi-index are provided. The main contribution of this study is as follows:

- A sensitivity analysis of seven key parameters for four different layouts of the Brayton cycle was carried out to determine the decision variables and their range of values. The influence of the design parameters on the thermodynamics and economics of the system was analyzed.
- Taylor diagrams were used to evaluate the Pareto compromise solutions determined by the four MADM methods and to determine the unique optimal solution.
- The G1 + TOPSIS method was used to comprehensively evaluate the optimization results by comparing 16 schemes comprising four nuclear reactors and four layouts in terms of safety, compactness, thermal, and economic performances. The characteristics and final

ranking of each scheme are also given. Decision-makers can make scheme choices based on demand.

2 System layouts and assumptions

This study uses four different layouts of the Brayton cycle for optimization. One of the most basic cycle layouts is the simple recuperation cycle (SR). It consists of a turbine (Turb), a heat exchanger (HX), a recuperator (RC), a pre-cooler (PC), a compressor, and a generator, as shown in Fig. 1. The working fluid is heated in the recuperator (state points 2–3) after being compressed near the critical point (state points 1–2) and then reheated by the cooling medium of reactor coolant in the heat exchanger (state points 3–4). At this point, the working fluid, which has a high enthalpy

at the heat exchanger outlet, will expand in the turbine to do work and drive the generator to produce electricity (state points 4–5). The expanded working fluid is then cooled on the low-pressure side of the recuperator (state points 5–6) and further cooled by exchanging heat with cooling water in the pre-cooler before being compressed again (state points 6–1).

Figure 2 shows the recompression cycle (RC), which has one more recompressor and recuperator than the simple recuperation cycle. In the recompression cycle, the working fluid is split at the outlet of the low-temperature recuperator (LTR) (state point 8), part of the fluid enters the pre-cooler (state points 2–3), and the rest enters the recompressor (state points 8–3b), finally converging at the high-pressure inlet side of the high-temperature recuperator (state point 3b). As the specific heat capacity of the fluid on the low-pressure

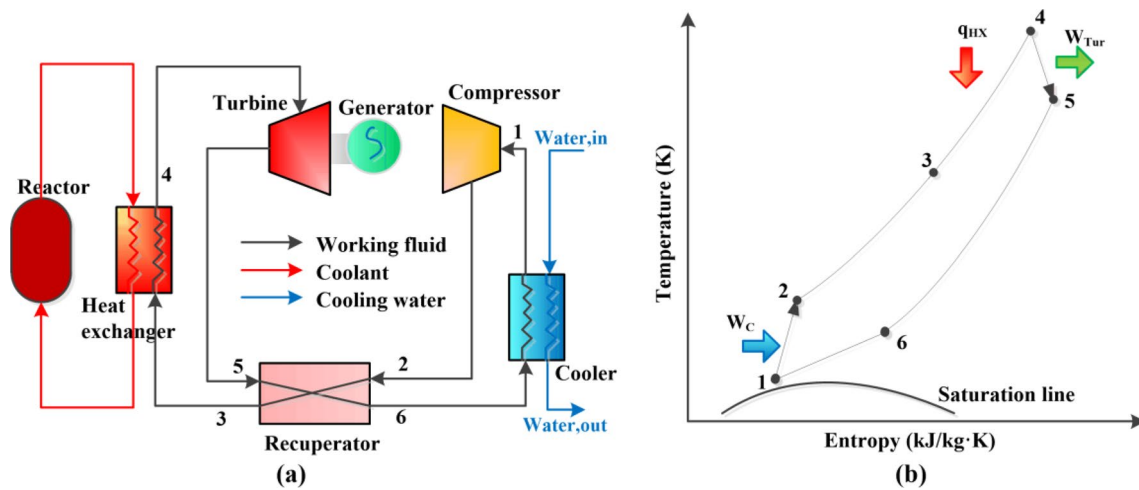


Fig. 1 (Color online) a Schematic and b T–S diagram of a simple recuperation cycle (SR)

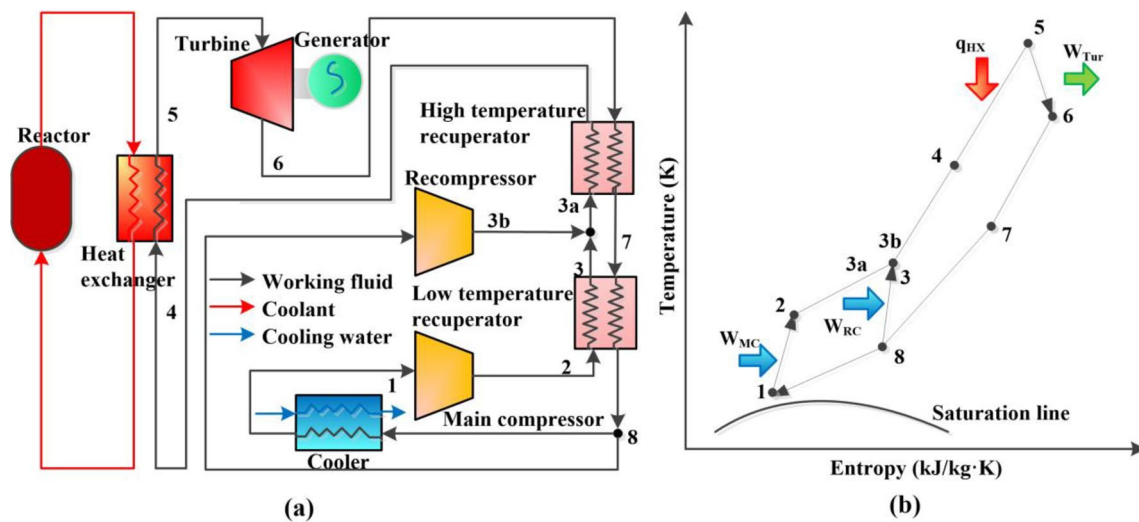


Fig. 2 (Color online) a Schematic and b T–S diagram of the recompression cycle (RC)

side of the recuperator is less than that on the high-pressure side, increasing the mass flow rate of the fluid on the low-pressure side can balance the specific heat capacity on both sides of the recuperator, enhancing heat recovery and avoiding the pinch point.

The other two-cycle layouts are the reheating cycle and the intercooling cycle. As shown in Figs. 3 and 4, the working fluid is heated and expanded twice in the reheating cycle (state points 4–5 and 6–7), which means that more expansion work (W_{tur1} and W_{tur2}) can be produced for the same compression work input (W_c), resulting in a higher net output work and cycle efficiency. The intercooling cycle regulates the minimum pressure (P_1) and intermediate pressure (P_8) of the cycle using secondary

compression and intercooling, thus reducing the required compression work (W_{c1} and W_{c2}) to increase the cycle efficiency.

Several general assumptions are made to simplify the simulation, as follows:

- (1) The S-CO₂BC operates in the steady state.
- (2) The heat losses are neglected during each part of the experiment.
- (3) The cooling water used in the cooler is in the environmental state.
- (4) The resistance loss of the pipeline is ignored.

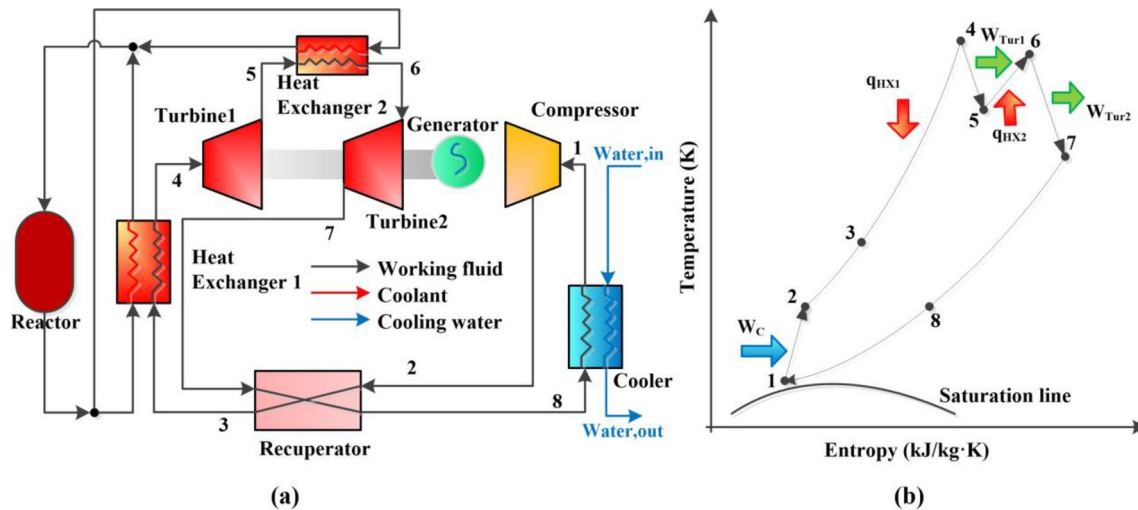


Fig. 3 (Color online) a Schematic and b T-S diagram of the reheating cycle (RH)

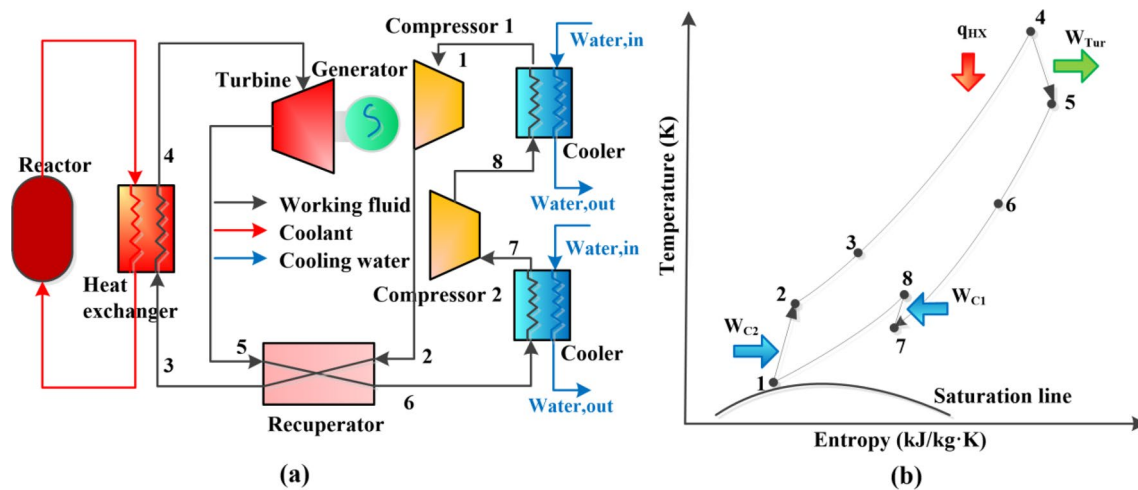


Fig. 4 (Color online) a Schematic and b T-S diagram of the intercooling cycle (IC)

3 Methodology description

A comprehensive multi-index evaluation and optimization method based on designing power conversion systems for nuclear power plants can guide decision-makers. As shown in Fig. 5, the method is based on the hierarchical analysis method, which consists of the scheme hierarchy (four nuclear reactors and four-cycle layouts), the index hierarchy (consisting of 11 indices at four levels), and the target hierarchy. (The best scheme can be evaluated based on the actual needs of decision-makers.) The data in the index hierarchy are obtained from the model layer. Before the final evaluation, it is necessary to optimize each scheme to ensure the accuracy of the evaluation. The optimization process mainly uses the NSGA-II algorithm to obtain the Pareto optimal frontier. Then, four multi-attribute decision methods are used to obtain the compromise schemes. Finally, the optimal results of each scheme were obtained by comparing the four compromise schemes through Taylor diagrams. The optimal results are evaluated to obtain the optimal scheme.

3.1 Fundamental model

This section presents the thermodynamic model, the heat exchanger thermal-hydraulic model, and the techno-economic model for the nuclear Brayton cycle system. The models are mainly constructed by calling the NIST REFPROP database through the simulation program.

3.1.1 Thermodynamic model

A thermodynamic model was constructed based on the first and second principles of thermodynamics. The energy calculations for the main components for all cycle layouts are given in Table 1. In Table 1, Q represents the heat transfer flow rate, W represents output/input power, and h represents enthalpy.

For the recompression cycle, the total input power of the main compressor and recompressor can be expressed as:

$$W_{MC} = m_f(h_{MC,out} - h_{MC,in})SR \tag{1}$$

$$W_{RC} = m_f(h_{RC,out} - h_{RC,in})(1 - SR) \tag{2}$$

where SR is the system circulation diversion ratio.

In the reheating cycle, as shown in Fig. 3, the reactor cooling fluid is divided equally into two parts, which are heated in turn to the working fluid and then converge and enter the reactor, and the heat transfer flow rate between the two times is expressed as:

$$Q_{HX1} = m_f(h_4 - h_3) = 0.5m_R c_p(T_{R,in} - T_{R,out,1}) \tag{3}$$

$$Q_{HX2} = m_f(h_6 - h_5) = 0.5m_R c_p(T_{R,in} - T_{R,out,2}) \tag{4}$$

$$\Delta T_{cf} = (T_{R,out,2} - T_{R,out,1})/2 \tag{5}$$

where c_p is the specific heat capacity of the reactor cooling fluid and ΔT_{cf} is the confluence temperature difference of the reactor cooling fluid.

The net output work of the S-CO₂BC system:

$$W_{net} = W_{Tur} - W_C \tag{6}$$

The thermal efficiency of the S-CO₂BC system:

$$\eta_t = W_{net} / Q_{HX} \times 100\% \tag{7}$$

Exergy is the part of the energy that can do work, and the exergy destruction is inevitable in the actual process. Exergy efficiency is an effective method to evaluate the supercritical Brayton cycle. The exergy of each state point can be calculated by:

$$E_i = m[(h_i - h_0) - T_0(s_i - s_0)] \tag{8}$$

$$E_{in} = Q_{HX}(1 - T_0/T_R) \tag{9}$$

where m denotes the working fluid mass flow rate, h_i and s_i are the specific enthalpy and entropy at each point, and 0 refers to the environment state. T_R is the temperature of the coolant that enters HX to provide heat for the cycle (Fig. 5).

The cycle exergy efficiency is defined as:

$$\eta_e = W_{net} / E_{in} \tag{10}$$

Table 1 Calculation of energy of main components

Components	Energy
Heat exchanger	$Q_{HX} = m_f(h_{HX,out} - h_{HX,in}) = m_R c_p(T_{R,in} - T_{R,out})$
Recuperator	$Q_{Recup} = m_{f,H}(h_{H,in} - h_{H,out}) = m_{f,L}(h_{L,out} - h_{L,in})$
Turbine	$h_{Tur,out} = (h_{Tur,out,is} - h_{Tur,in})\eta_T + h_{Tur,in}$ $W_{Tur} = h_{Tur,out} - h_{Tur,in}$
Compressor	$h_{C,out} = (h_{C,out,is} - h_{C,in})/\eta_C + h_{C,in}$ $W_C = h_{C,out} - h_{C,in}$

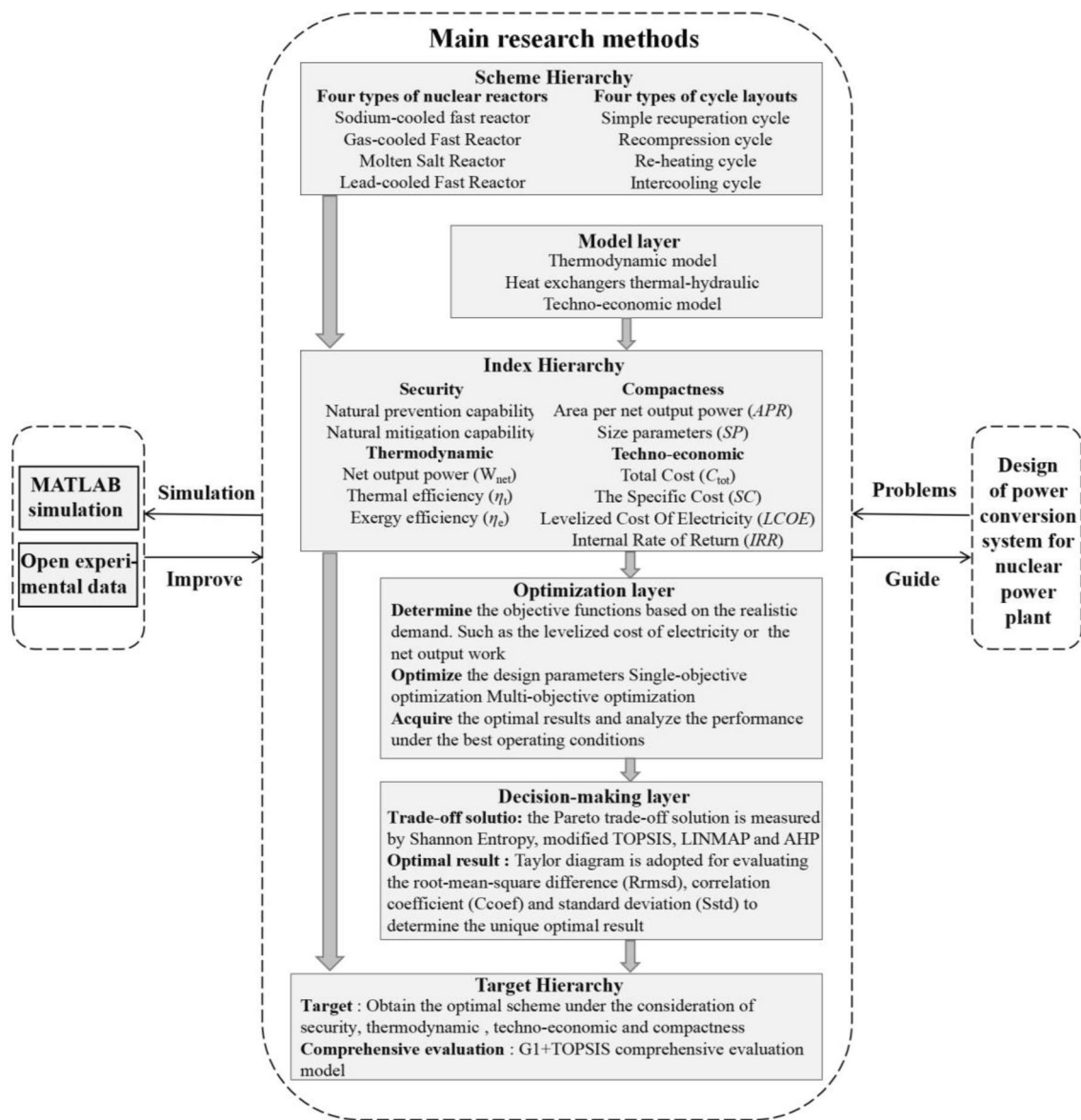


Fig. 5 Description of comprehensive multi-index evaluation and optimization method

3.1.2 Heat exchangers' thermal–hydraulic model

PCHEs were chosen for the heat exchange thermal–hydraulic model because they have been adopted in many studies on SCO₂-based power cycles due to their compact size and ability to withstand high pressures. A model similar to that proposed in Dostal's Thesis [32] is used in this work. According to the assumptions established in Ref. [32], it is sufficient to model a pair of hot and cold channels rather than the entire core of the PCHÉ. PCHÉs adopt a semi-circular straight channel model [33]. Figure 6 shows the structural diagram of a heat exchange unit.

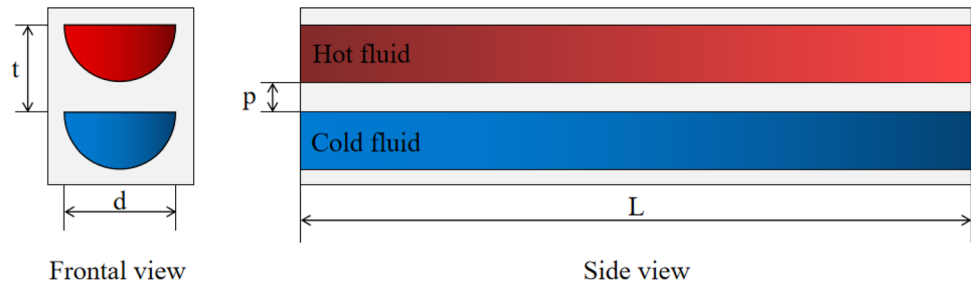
The logarithmic mean temperature difference (LMTD) method was used to calculate the heat transfer area, as

indicated in Eq. (11). The total heat transfer coefficient was calculated using the contributions of the thermal resistances by conduction and convection [Eq. (12)], and the convective heat transfer coefficient was calculated using Eq. (13), where D is the hydraulic diameter. The calculation formula is shown in Eq. (14), and the Reynolds number is calculated using Eq. (15).

$$Q = UA\Delta T_{\text{lmtd}} \quad (11)$$

$$\frac{1}{U} = \frac{1}{\alpha_{\text{hot}}} + \frac{t}{\lambda} + \frac{1}{\alpha_{\text{cold}}} \quad (12)$$

Fig. 6 Structure diagram of PCHE



$$\alpha = \frac{Nuk}{D} \tag{13}$$

$$D = \frac{4\pi d^2}{8\left(\frac{1}{2}\pi d + d\right)} \tag{14}$$

$$Re = \frac{GD}{\mu} \tag{15}$$

For the hydraulic model, only pressure drops due to friction were considered. The well-known Darcy–Weisbach equation [Eq. (16)] was applied in each segment. The total pressure drop for each channel is given by Eq. (27).

In Appendix, the equations used to calculate the Nusselt number (Nu) and the friction factor (*f*) are presented. It is worth noting that in PCHE, the relative roughness δ of the pipe is the ratio of the surface roughness ϵ ($\epsilon = 10^{-3}$ is used in this study) [32] to the pipe diameter *d*.

$$\Delta P = f \frac{L}{D} \rho \frac{V^2}{2} + C\rho \frac{V^2}{2} \tag{16}$$

3.1.3 Model validation

This study intends to establish and verify the model through simulation software based on the data of the advanced burner test reactor preconceptual design report provided by Argonne National Laboratory in the United States [33]. This experiment is a performance study of the sodium-cooled fast reactor coupled with the S-CO₂ recompression Brayton cycle (RC); the reactor cooling medium is metallic sodium. The initial parameters for cycle simulation are given in Table 2 and 3 for validation. The comparison between the model established in this study and the experimental parameters in the references is shown in Fig. 7 and Table 4. The errors of entropy and temperature at each point of the cycle are guaranteed to be within 3%, which verifies the model’s accuracy. Therefore, the model can be used for further parameter analysis and optimization.

Table 2 Setting parameters in the experiment [33]

Term	Value
Turbine inlet temperature, T_{\max} (K)	744.95
Main compressor inlet temperature, T_{\min} (K)	304.4
Main compressor inlet pressure, P_{\min} (MPa)	31.25
Main compressor outlet pressure, P_{\max} (MPa)	7.4
Turbine isentropic efficiency, η_T	0.934
Main compressor isentropic efficiency, η_{MC}	0.891
Recompressor isentropic efficiency, η_{RC}	0.875
Environment temperature, T_0 (K)	303.15
Environment pressure P_0 (MPa)	0.1
Shunt ratio, SR	0.71
Reactor power, Q_r (MWt)	250
Sodium mass flow, m_r (Kg/s)	1259
Sodium inlet temperature, $T_{r,in}$ (K)	761.15
Sodium outlet temperature, $T_{r,out}$ (K)	606.15

Table 3 Geometric parameters of PCHE [33]

	<i>T</i> (mm)	<i>d</i> (mm)	<i>p</i> (mm)	<i>L</i> (m)
Heat exchanger	2.0	2	2.4	1
Recuperator	2	1.5	2.3	0.6
Cooler	1.66	2.0	2.4	0.593

3.1.4 Techno-economic model

Four economic indices and two compactness indices have been adopted in this study to holistically assess the techno-economics of the nuclear Brayton cycle holistically. Specifically, these include the heat transfer area per net output power (APR) and the turbine characteristic size parameter (SP), which represents compactness, and C_{tot} , SC, LCOE, and IRR, which represent economy.

The heat transfer area per net output power (APR), which is the ratio of heat exchange area to net output work, is used as an evaluation criterion for the compactness of the heat exchanger. APR is defined as:

$$APR = (A_{\text{HX}} + A_{\text{RC}} + A_{\text{C}}) / W_{\text{net}} \tag{17}$$

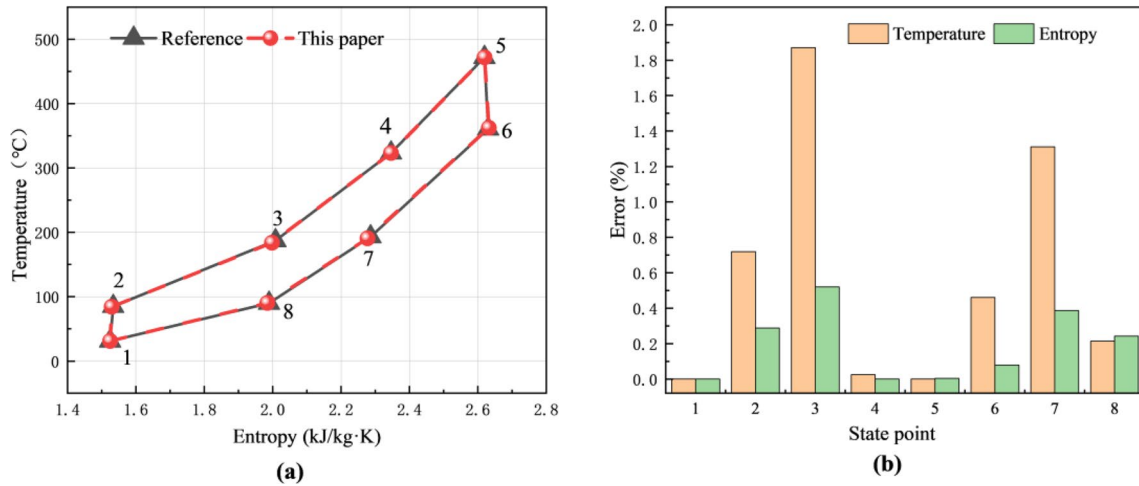


Fig. 7 (Color online) Validation of the constructed S-CO₂BC model

Table 4 Comparison between the results calculated using the established model and the data from Ref. [33]

Parameters	Reference	Calculated	Error (%)
Working fluid (CO ₂) mass flow rate, m_f (kg/s)	1377	1371.4	0.4
Compressor input power, W_C (KW)	53,151	56,114	5.57
Turbine output power, W_{Tur} (KW)	157,530	159,570	1.29
Cooler outlet water temperature, $T_{Water, out}$ (°C)	35.8	36.5	1.95
Thermal efficiency, η_t (%)	41.6	41.41	0.46

Table 5 Method of calculating the cost of system components

Components	Capital investment cost function	data sources
Reactor	$Z_R = C_{in} Q_r, \quad C_{in} = 283 \text{ \$/kW}_{th}$	[34]
Turbine	$C_T = 479.34 m_T \left(\frac{1}{0.93 - \eta_T} \right) \ln(\beta_T) (1 + \exp(0.036 T_T - 54.4))$	[35]
Compressors	$C_c = 71.1 m_{in} (1/0.92 - \eta_c) PRC \cdot \ln(PRC)$	[35]

The turbine characteristic size parameter (SP) is an index used to evaluate the ease and compactness of turbine manufacturing. The smaller the SP, the more compact the turbine structure. It is defined as:

$$SP = \sqrt{V_{Tur}} / \Delta h_{isen}^{0.25} \tag{18}$$

where V_{Tur} denotes the volume flow rate of the working fluid in the turbine, Δh_{isen} denotes the isentropic enthalpy drop at the inlet and outlet of the working fluid of the turbine.

The specific cost (SC) represents the average investment cost of the unit power output of the power plant and is defined as:

$$SC = \frac{C_{tot}}{W_{net}} \tag{19}$$

$$C_{tot} = \left(C_R + \sum_{j=1}^N C_{PCHE,j} + \sum_{j=1}^N C_{Tur,j} + \sum_{j=1}^N C_{C,j} \right) C_{inst} \tag{20}$$

where C_{tot} is the total investment cost, considering the equipment cost (including reactor, PCHE, compressor, and turbine) and the auxiliary equipment and installation cost. C_{inst} is the auxiliary installation cost index.

The cost of PCHE is calculated by referring to the calculation method in Dr Dostal and the quotation of Heatric (30 \$/kg for stainless steel units) [32], calculating the weight of PCHE to estimate its cost. The formula for calculating the weight of the PCHE is given in Eqs. (21) and (22).

$$M_{PCHE} = V_{PCHE} \cdot f_m \cdot \rho \tag{21}$$

$$f_m = 1 - \frac{\pi d^2}{8Pt} \tag{22}$$

where V_{PCHE} denotes the volume of the PCHE and f_m represents the actual volume per cubic meter of the heat exchanger. The cost calculation method for other parts is shown in Table 5. Notably, among the costs calculated by these formulas, the heat exchangers and reactors cost the equivalent of 2003 dollar values, while the remaining components cost the equivalent of 1994 dollar values [32]. This study converts the calculated cost multiplied by the inflation factor to the cost at the end of 2022. Inflation data for the US power sector show that the inflation rates for 1994 and 2003 to 2022 are 78.29% and 60.78%, respectively.

The levelized cost of electricity (LCOE) is the cost of generating electricity over the full life cycle of the power plant, defined as:

$$LCOE = \frac{PVE}{8760u \cdot NY \cdot W_{net}} \tag{23}$$

$$PVE = C_{tot} + \sum_{k=1}^{NY} \frac{CF_{xp,k}}{(1+r)^k} \tag{24}$$

$$CF_{xp,k} = W_{net} (OM(1+er)^k) \tag{25}$$

The internal rate of return (IRR) is defined as:

$$-C_{tot} + \sum_{k=1}^{NY} \frac{CF_{rev,k} - CF_{xp,k}}{(1+IRR)^k} = 0 \tag{26}$$

$$CF_{rev,k} = W_{net} (8760 \cdot u \cdot C_e (1-dr)^k) \tag{27}$$

The data required to calculate the economic indices are shown in Table 6.

Table 6 Assumptions in the economic calculation [36]

Plant	Data
Plant installation cost, C_{inst}	1.3
O&M operations, OM (\$/kWe)	30
Escalation rate, er (%)	3
Plant degradation rate, dr (%)	1
Electricity market price, C_e (\$/kWh)	0.06
Plant lifetime, NY (years)	20
Plant utilization factor, u (%)	85
Discount rate, r (%)	5

3.2 Multi-objective optimization model

Compared to single-objective optimization, multi-objective optimization can optimize two or more mutually constrained objectives simultaneously. This study used the non-dominant sorting genetic algorithm NSGA-II to optimize two contradictory objectives: η_t (thermodynamic performance) and LCOE (economic performance). The turbine inlet temperature T_{max} , main compressor outlet pressure P_{max} , turbine efficiency, compressor efficiency η_C , split ratio SR (only for recompression cycle), confluence temperature difference ΔT_{cf} (only for reheating cycle) and primary compression pressure P_{pr} (only for intercooling cycle) were selected as the decision variables for optimization. Therefore, the multi-objective optimization model can be expressed as:

$$\begin{cases} \max(\eta_t) = f_1(P_{max}, T_{max}, \eta_T, \eta_C, SR, \Delta T_{cf}, P_{pr}) \\ \min(LCOE) = f_2(P_{max}, T_{max}, \eta_T, \eta_C, SR, \Delta T_{cf}, P_{pr}) \end{cases} \tag{28}$$

The NSGA-II method is based on a genetic algorithm and the Pareto optimal concept. It is a commonly used multi-objective optimization algorithm whose basic idea is to generate different sets of decision variables (also called individuals) within a certain range and to use these sets of variables to calculate thermodynamic and techno-economic metrics. By evaluating and ranking the objective functions, NSGA-II can analyze each optimal solution and the suboptimal solutions adjacent to them according to the value of the objective function and plot these solutions on a Pareto frontal map to help decision-makers find an equilibrium point to achieve multi-objective optimization. The main parameters of the NSGA-II are listed in Table 7. These parameters are used to control the execution of the algorithm and influence the quality and computational efficiency of the solution.

3.3 Decision-making methods (DMM)

After NSGA-II optimization, only an optimal solution set can be obtained. Further, Pareto compromise solutions

Table 7 Input parameters of NSGA-II

Parameters	Value
Population size	100
Maximum generation	120
Crossover probability	0.8
Mutation probability	0.2
Selection function	Binary tournament
Objective functions	LCOE(min), η_t (max)
Decision variables	$P_{max}, T_{max}, \eta_C, \eta_T, SR, \Delta T_{cf}, P_{pr}$

must be obtained to obtain a unique solution. Previous studies have shown a large variation in the Pareto compromise solution obtained by different decision methods, making it impossible for decision-makers to judge which method obtains the desired results. Therefore, this study uses various decision methods, including Shannon entropy, a modified technique for order preference by similarity to ideal solution (TOPSIS), linear programming techniques, multidimensional analysis preference (LINMAP), and the analytic hierarchy process (AHP) to determine four Pareto compromise solutions. Finally, Taylor diagrams are used to evaluate the priority of these compromise solutions to obtain the final Pareto optimal compromise solution.

3.3.1 DMM1: Shannon entropy model

The basic idea of the Shannon entropy method is to determine the optimal solution by calculating the information entropy value of each solution to measure its stochasticity and uncertainty. A smaller information entropy value indicates a more deterministic and reliable solution and, conversely, a more uncertain and stochastic solution.

Normalization of the decision-making matrix:

$$E_{ij} = \frac{F_{ij}}{\sum_{i=1}^n F_{ij}}, i = 1, 2, \dots, n, j = 1, 2, \dots, m \quad (29)$$

where E_{ij} is the objective value, i and j represent the quantities of the scheme and objective function.

The Shannon entropy is defined as:

$$H_j = -\frac{1}{\ln(n)} \sum_{i=1}^n E_{ij} \ln E_{ij} \quad (30)$$

Equation (31) evaluates the weight of the objective. Equation (32) calculates the matrix of solutions sorted in descending order after decision-making. Shannon entropy point is searched from the W_i , which ranked first.

$$w_j = (1 - H_j) / \sum_{j=1}^m (1 - H_j) \quad (31)$$

$$W_i = E_{ij} \cdot w_j \quad (32)$$

3.3.2 DMM2 and DMM3: modified TOPSIS and LINMAP model

The shortest Euclidean distance between the Pareto optimal solution and the longest distance with the nadir point identifies the traditional (TOPSIS) points. The limitation of this method is that there may be two TOPSIS

decision-making points at different locations. For this reason, relative entropy is introduced in this study to correct it.

Positive $Z^+ = (z_1 + 1, z_2 + 2, \dots, z_n + n)$ and negative $Z^- = (z_1 - 1, z_2 - 2, \dots, z_n - n)$ ideal solutions are explained as below:

$$z_j^+ = \max_{1 \leq i \leq n} \{R_{ij}\} z_j^- = \min_{1 \leq i \leq n} \{R_{ij}\}, \quad \text{for the higher the better criteria} \quad (33)$$

$$z_j^+ = \min_{1 \leq i \leq n} \{R_{ij}\} z_j^- = \max_{1 \leq i \leq n} \{R_{ij}\}, \quad \text{for the lower the better criteria} \quad (34)$$

Relative entropy distance is calculated as:

$$D_i^+ = \sum_{j=1}^m \left\{ z_j^+ \lg \frac{z_j^+}{R_i} + (1 - z_j^+) \lg \frac{1 - z_j^+}{1 - R_i} \right\} \quad (35)$$

$$D_i^- = \sum_{j=1}^m \left\{ z_j^- \lg \frac{z_j^-}{R_i} + (1 - z_j^-) \lg \frac{1 - z_j^-}{1 - R_i} \right\} \quad (36)$$

The modified TOPSIS point is selected according to the maximum coefficient T_i :

$$T_i = \frac{D_i^-}{D_i^- + D_i^+} \quad (37)$$

Based on the relative entropy, the modified LINMAP point is defined as:

$$L_i \in \min(D_i^+) \quad (38)$$

3.3.3 DMM4: AHP model

Compared to the previous methods, AHP (analytic hierarchy process) is a subjective weighting method. It allows for defining the weight of the objective values in decision-making according to the decision-maker's preference. The judgment matrix constructed for the Pareto frontier is defined as:

$$a_{ij} = \frac{i}{j} \quad (39)$$

where i and j represent the importance of the corresponding indices, and the importance of the thermodynamic, technical, and compactness indices are 3, 2, and 1, respectively, for this study. The weight matrix of the AHP method is defined as:

$$\omega_j = \left(\prod_{j=1}^n a_{ij} \right)^{\frac{1}{n}} / \sum_{k=1}^n \left(\prod_{j=1}^n a_{kj} \right)^{\frac{1}{n}} \quad (40)$$

The normalization matrix constructed by the AHP method is the same as that of the Shannon entropy model, with specific reference to Eq. (29). The final decision matrix, Eq. (41), is obtained by multiplying the two. The AHP point is searched based on the A_i , which ranked first.

$$A_i = E_{ij} \cdot \omega_j \tag{41}$$

3.3.4 Taylor diagram evaluation model

Taylor diagrams [37] are a graphical technique for comparing performance differences between multi-objective optimization solutions. Taylor diagrams allow the performance metrics of multiple solutions to be plotted in the same coordinate system to visualize the differences between them. The performance metrics include root-mean-square difference (R_{rmsd}), correlation coefficient (C_{coef}), and standard deviation (S_{std}). The specific formulas are expressed as:

$$R_{\text{rmsd}} = \sqrt{\frac{1}{n} \sum_{i=1}^n [(f_i - \bar{f}) - (r_i - \bar{r})]^2} \tag{42}$$

$$C_{\text{coef}} = \frac{\sum_{i=1}^n (f_i - \bar{f})(r_i - \bar{r})}{\sqrt{\sum_{i=1}^n (f_i - \bar{f})^2} \sqrt{\sum_{i=1}^n (r_i - \bar{r})^2}} \tag{43}$$

$$S_{\text{std}} = \sqrt{\frac{1}{n} \sum_{i=1}^n (f_i - \bar{f})^2}, \quad S_{\text{std},r} = \sqrt{\frac{1}{n} \sum_{i=1}^n (r_i - \bar{r})^2} \tag{44}$$

3.4 Final evaluation model: G1 + TOPSIS

The optimal result for each solution can be obtained after performing multi-objective optimization. In order to comprehensively compare the advantages and disadvantages

of each scheme, in this study, the G1 [38] (ordinal relation analysis method) + TOPSIS comprehensive evaluation model is established. The four reactors and four-cycle layouts are compared in all aspects, including safety, thermodynamics, economics, and compactness. The safety problems of nuclear reactors are related to aspects that this study has not discussed deeply. This study refers to Bertrand et al. [4] for the safety assessment of Generation IV nuclear reactors. The safety of different nuclear reactors is scored in terms of Natural prevention capability for each concept and Natural mitigation capability for each concept. Notably, Ref. [4] does not assess the safety of lead-cooled fast reactors, and this study combines the evaluation of the safety of Gen IV reactors by Kelly [39] and Tuček et al. [6] to finalize the values of indexes C1 and C2. The concept scores for prevention and mitigation are shown in Table 8. Table 9 shows all the indexes used for the evaluation. The evaluation process is shown in Fig. 8.

The TOPSIS model is described in Sect. 3.3.2. The ordinal relation analysis method (G1) uses the weighting between each criterion layer. The following briefly describes the steps in the G1 method when determining weights.

Table 9 Comprehensive evaluation indices

Criterion	Indexes
Security (B1)	Natural prevention capability (C1) Natural mitigation capability (C2)
Thermodynamic (B2)	W_{net} (C3) η_t (C4) η_e (C5)
Economy (B3)	C_{tot} (C6) SC (C7) LCOE (C8) IRR (C9)
Compactness (B4)	PBP (C10) APR (C11)

Table 8 Reactor concept scores for prevention and mitigation (x and + means multiplying and adding indicators of the same box) [4]

Prevention indicators/concept	GFR	SFR	LFR	MSR
Loss of heat sink	31	31	31	33
(Unprotected) loss of flow accident/loss of coolant accident	21	21	21	11
TOP margin to prompt-criticality x power increase dynamics	11	32	32	11
Passive cooling conduction	11	13	11	33
Prevention total score	1.9	3.9	3.9	5.6
Cladding loading in sub-assembly thermomechanical + chemical	33	22	22	13
Primary boundary thermal loading	13	13	13	21
Containment loading mechanical (static) + mechanical (dynamic)	23	33	23	11
Fission product release inventory x confinement/retention	12	32	32	22
Mitigation total score	6.3	7.4	6.8	4.8

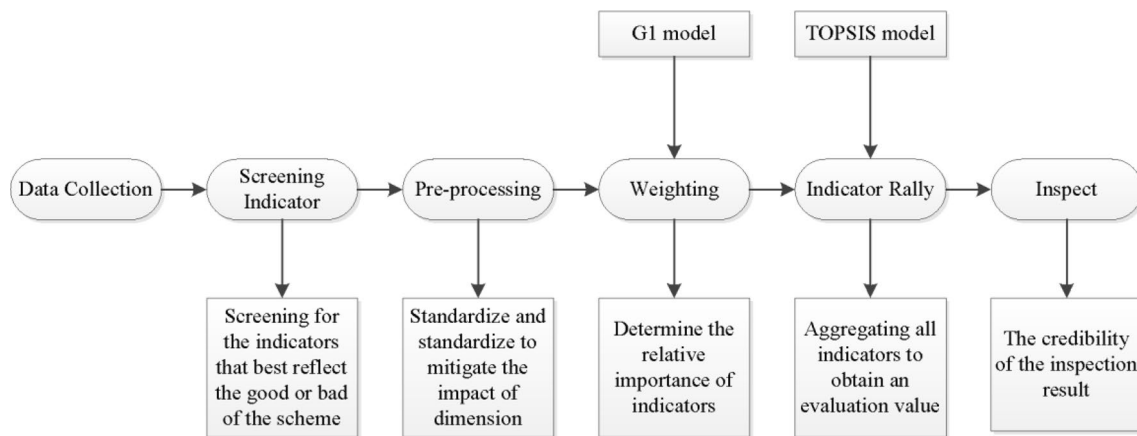


Fig. 8 G1 + TOPSIS comprehensive evaluation process

Table 10 Main parameters of the reactor

	GFR [40]	SFR [41]	LFR [42]	MSR [42]
Power rating (MWt)	2400	2400	2400	2400
Coolant	S-CO ₂	Sodium	Lead	NaCl–KCl–MgCl ₂ salt
Primary system pressure (MPa)	20	0.1	0.1	0.1
Core inlet temperature (°C)	485.5	371	479	496
Core outlet temperature (°C)	650	510	573	581
Core flow rate (Kg/s)	11,708	13,580	173,600	29,000
Power conversion system	S-CO ₂	S-CO ₂	S-CO ₂	S-CO ₂

Step 1 Determine the ranking relationship of each index according to the importance of each evaluation index in the research object. The ranking determined in this study is B1 > B2 > B3 > B4. Their relative importance was 1.6, 1.2, and 1.4, respectively.

Step 2 Give a comparative judgment of the relative importance between adjacent indexes and assign a value:

$$r_k = \frac{w_{k-1}}{w_k} \quad (k = n, n-1, \dots, 2) \quad (45)$$

where, n is the total number of evaluation indexes.

Step 3 Calculate the index weights w_k , and give the Rational assignment w_k subjectively.

$$w_n = \left(1 + \sum_{k=2}^n \prod_{i=k}^n r_i \right)^{-1} \quad (46)$$

$$w_{k-1} = r_k w_k \quad (k = n, n-1, \dots, 2)$$

The set of weights derived by the G1 method is $(w_1, w_2, \dots, w_n)^T$.

The final score for each scheme is the sum of the index score for each criterion level multiplied by the weights.

Table 11 Conditions of the simulation

Input parameters	Value
Compressor inlet temperature, T_{\min} (K)	304.4
Compressor inlet pressure, P_{\min} (MPa)	31.25
Compressor outlet pressure, P_{\max} (MPa)	7.4
Turbine isentropic efficiency, η_T [43]	0.9
Compressor isentropic efficiency, η_C [43]	0.85
Environment temperature, T_0 (K)	303.15
Environment pressure, P_0 (MPa)[33]	0.1
Shunt ratio, SR	0.71

4 Results and discussion

This section focuses on the effect of seven key parameters on the thermal economy of a Brayton cycle system. The feasibility of four decision methods to obtain Pareto compromise solutions is analyzed. The differences in the thermo-economic indexes of each scheme before and after optimization are compared. Finally, the characteristics of each scheme are given by comprehensive evaluation. The

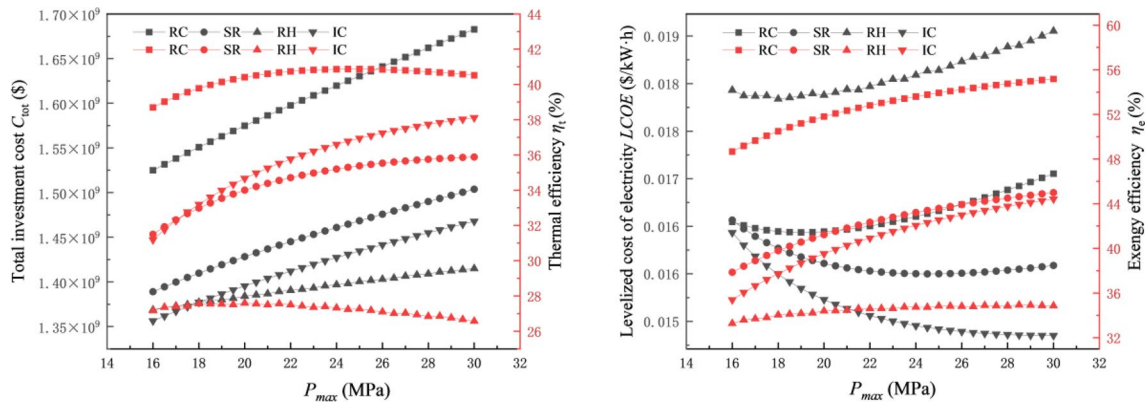


Fig. 9 Effect of main compressor outlet pressure (P_{max}) on system thermo-economic performance

main parameters used for the system simulation analysis are given in Tables 10 and 11. The specific parameters of PCHE can be obtained from.

4.1 Parametric analysis

Firstly, a single-objective parametric analysis was performed to determine the direction of the multi-objective optimization. The parameters on the heat source side of this section are analyzed using sodium-cooled fast reactors (SFR). Figure 9 shows the variation in the four indices representing thermodynamics and economy with compressor outlet pressure. As P_{max} increases, the total cost of the system and the exergy efficiency both show an increasing trend. For RC and RH, the system’s thermal efficiency increases and then reduces as P_{max} increases. The levelized electricity cost in the system reduces and then increases as P_{max} increases. The reason for this trend is that as the pressure increases, the enthalpy of the turbine inlet working fluid increases, leading to an increase in output power. However, simultaneously, the pressure-bearing requirements of the components increase,

the system’s total cost increases, and the cost increases faster than the system’s power output, meaning that there is an intermediate P_{max} at which η_t or LCOE of the system is optimized. Figure 10 shows that as P_{max} increases, the thermodynamic performance of the system increases, and the LCOE decreases. However, the initial investment cost (C_{tot}) also increases, meaning that the higher the system temperature within a certain range, the better the obtainable thermal and economic performances, but with a higher initial investment. Both the cycle efficiency and the cost of the system are influenced by the efficiency of the turbine (η_T) and the compressor (η_C), so this study analyzes their thermo-economic impact. Figures 11 and 12 show the effect of η_C and η_T on the thermo-economic performance of the system, and they have a similar impact on other system indices. Both system η_t and η_e increase as they increase, and the system’s thermodynamic performance is enhanced. The system’s total cost increases rapidly after η_T and η_C around 0.85. LCOE shows a decreasing trend and then increases, reaching a minimum at η_T and η_C around 0.85. Not the higher the η_T and η_C , the better it is. Decision-makers should consider this carefully.

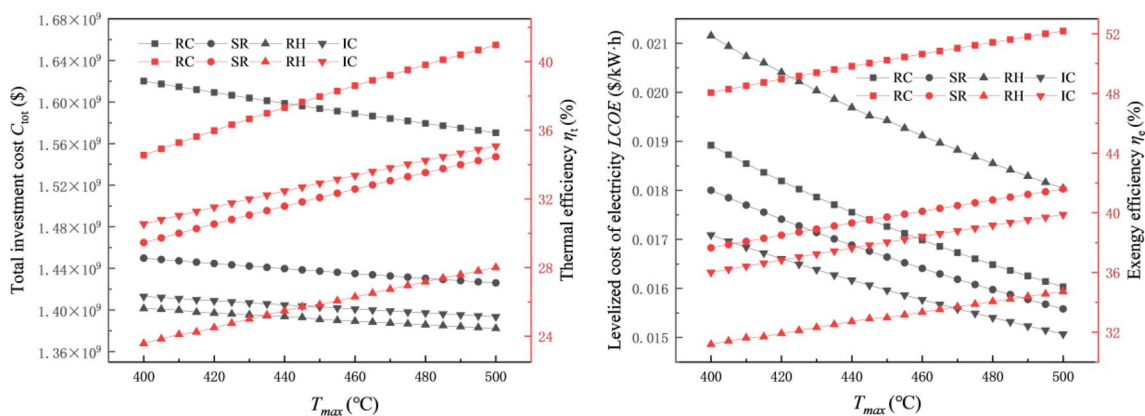


Fig. 10 Effect of turbine inlet temperature (T_{max}) on system thermo-economic performance

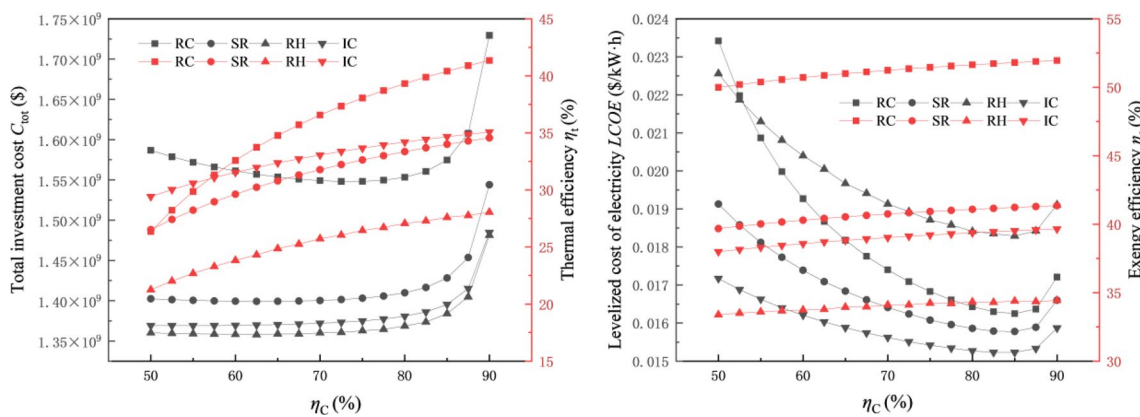


Fig. 11 Effect of compressor efficiency (η_c) on system thermo-economic performance

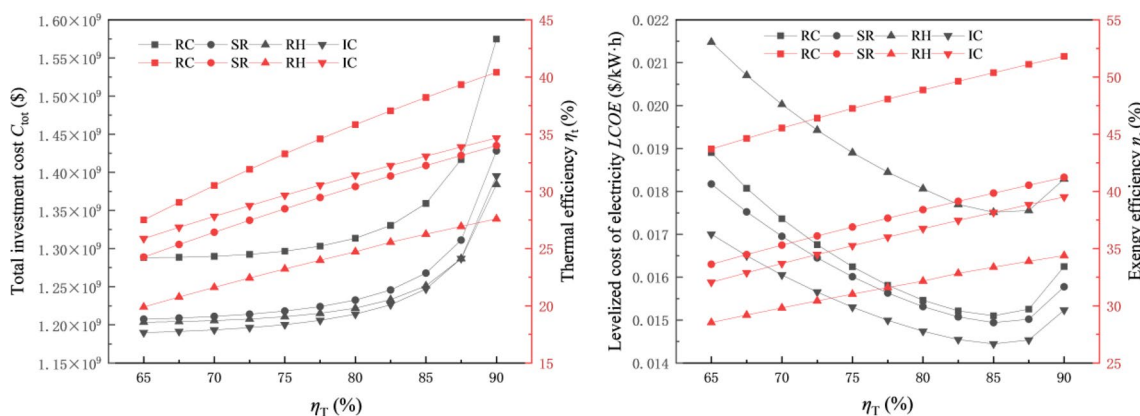
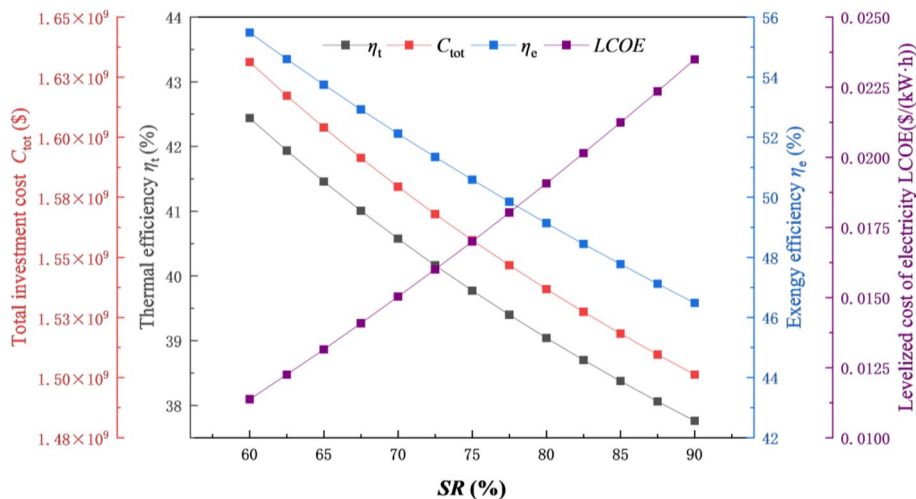


Fig. 12 Effect of turbine efficiency (η_T) on system thermo-economic performance

Fig. 13 Effect of shunt ratio (SR) on system thermo-economic performance



This study investigates specific RC, RH, and IC cycle parameters. Among them, the shunt ratio (SR) is an important parameter in the recompression cycle, and its influence on the thermo-economic of the cycle is shown in

Fig. 13. The effect of SR on the thermo-economic of the system is monotonic. As the thermodynamic performance of the system decreases with increasing SR, the system's total cost decreases. Nevertheless, the LCOE increases

with it, meaning that the smaller the SR within a certain range, the better, without considering investment costs. The ΔT_{cf} in the reheat cycle affects the operating temperature of the system. Therefore, it is necessary to study the ΔT_{cf} effect on the thermal properties of the system. As shown in Fig. 14, the thermodynamic performance and the system's economy increase with increasing ΔT_{cf} .

However, the system's total cost also increases. A proper primary compression pressure (P_{pr}) can bring lower input power to the system. The η_t and η_e junctions of the system decrease P_{pr} increases, which indicates that an increase in P_{pr} is not beneficial to the thermodynamic performance of the system. Also, LCOE tends to be unfavorable under the influence of P_{pr} (Fig. 15).

Fig. 14 Effect of confluence temperature difference (ΔT_{cf}) on system thermo-economic performance

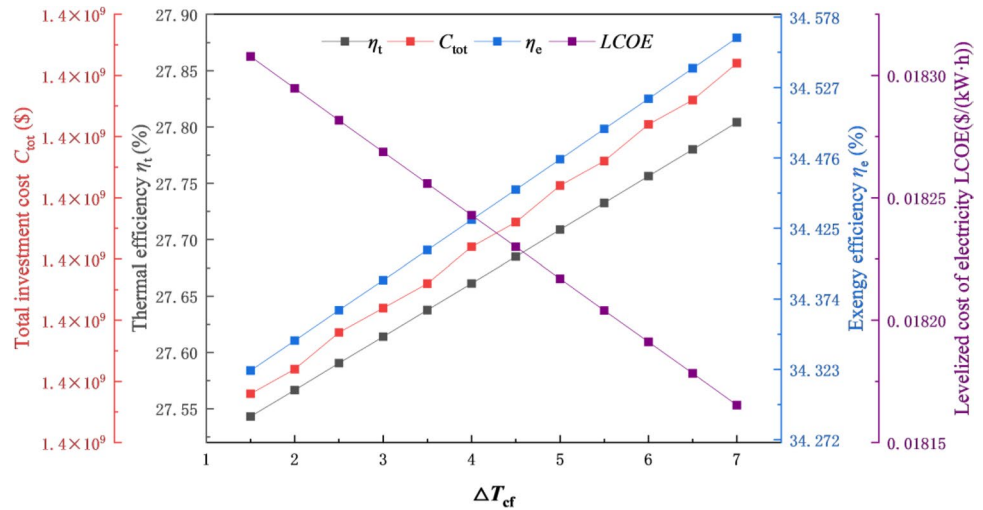


Fig. 15 Effect of primary compression pressure (P_{pr}) on system thermo-economic performance

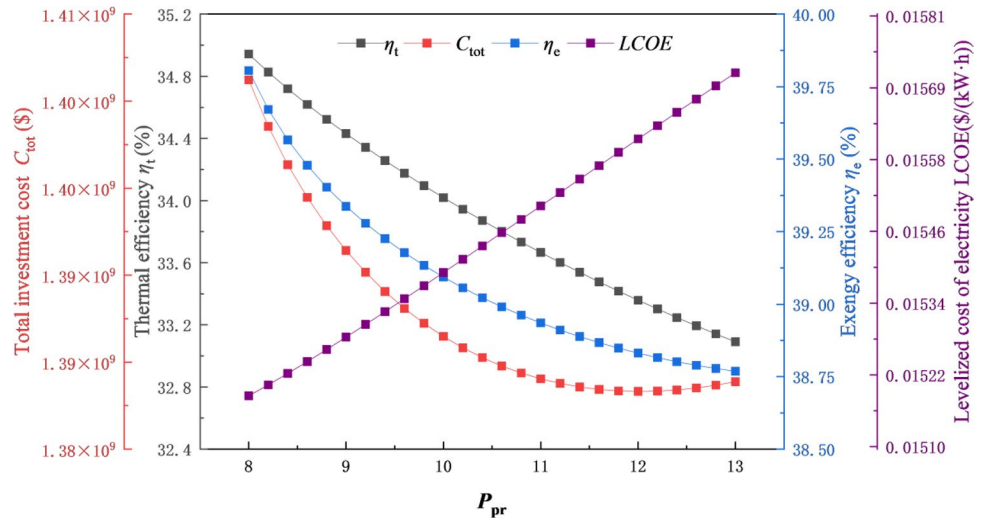


Table 12 Bounds of the decision variables

Parameters	GFR	SFR	LFR	MSR	Layouts
Compressor outlet pressure, P_{max} (MPa)	17–30	17–30	17–30	17–30	All
Turbine inlet temperature, T_{max} (K)	803.15–903.15	663.15–763.15	726.15–826.15	734.15–834.15	
Compressor efficiency, η_C	0.6–0.9	0.6–0.9	0.6–0.9	0.6–0.9	
Turbine efficiency, η_T	0.65–0.9	0.65–0.9	0.65–0.9	0.65–0.9	
Shunt ratio, SR	0.5–0.9	0.5–0.9	0.5–0.9	0.5–0.9	RC
Confluence temperature difference, ΔT_{cf} (K)	0–10	0–10	0–10	0–10	RH
Primary compression pressure, P_{pr} (MPa)	8–12	8–12	8–12	8–12	IC

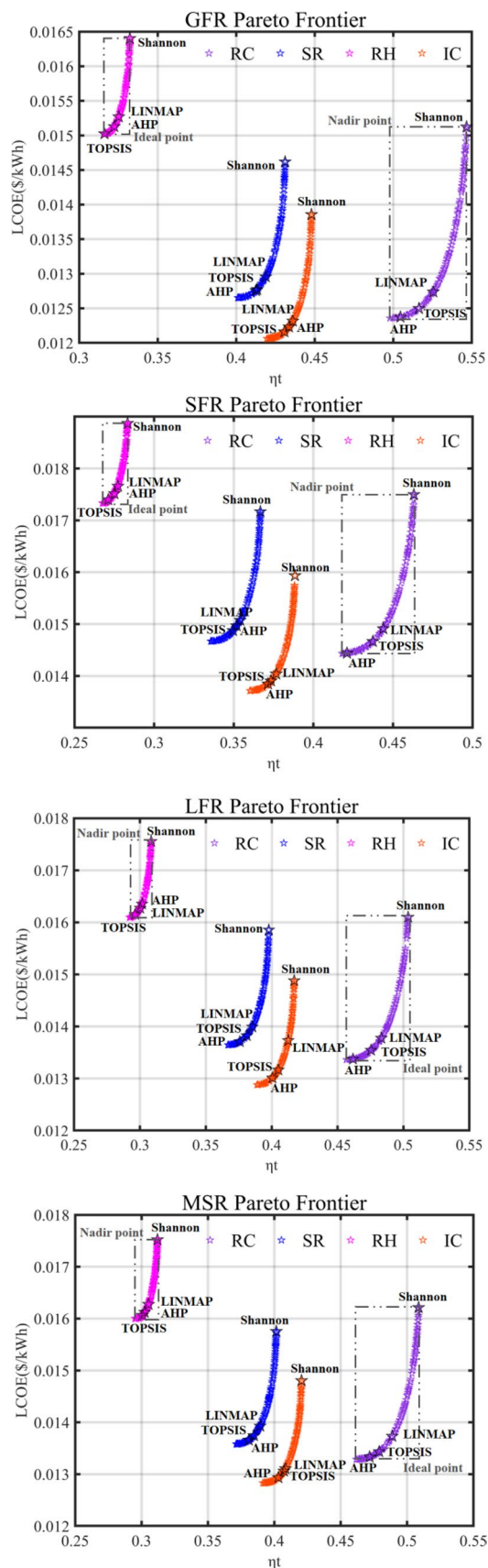


Fig. 16 (Color online) Pareto optimal frontier and four decision-making points

4.2 Multi-objective optimization results

From the analysis in Sect. 4.1, the cycle parameters P_{\max} and T_{\max} affect the system's thermodynamics and economy greatly, and the trends of the effects conflict with each other. This section conducts a multi-objective optimization study with these parameters as decision variables. The constraint conditions of the decision parameters of the cycle with multi-objective optimization are shown in Table 12, respectively. Figure 16 depicts the Pareto optimal frontier of a supercritical CO₂ Brayton cycle system using NSGA-II optimization for four nuclear reactors combined with four-cycle layouts. The optimization objectives are the net cycle efficiency (η_t) and the plant's levelized cost of electricity (LCOE). The LCOE increases moderately and then rapidly with the increase of η_t because the system-levelized cost of electricity increases faster than the net cycle efficiency at higher evaporation pressure and turbine inlet temperature. Similar results have been found in previous studies, where thermodynamic and techno-economic performance is mutually constrained, with higher thermodynamic performance leading to decreased techno-economic performance. Comparing the optimization results of different nuclear reactors, the highest η_t is for gas-cooled fast reactors, where the highest is for recompression cycles (RC), up to 54.67%, due to the higher core exit temperature of the GFR for the same thermal power of the reactor, resulting in a higher cycle efficiency. The LCOE of the intercooling cycle is the lowest at 0.1207\$/kWh, meaning that no single reactor type and cycle layout can achieve the techno-economic and thermodynamic performance optimum. The choice can be made according to different needs.

The ideal point of the Pareto frontier diagram is in the lower right corner outside the rectangular frontier, representing the theoretical goal of simultaneously obtaining the maximum η_t and the minimum LCOE. To determine the Pareto compromise solution, four decision methods, Shannon entropy, modified TOPSIS, LINMAP, and AHP, are applied in this study and compared on the Taylor diagram. Using Taylor diagrams, the final Pareto optimal solution is determined from these four decision points by measuring the root-mean-square difference, correlation coefficient, and standard deviation. Figure 16 shows the positions of the optimal solutions determined by different decision methods in the Pareto frontier. For the decision points, the Shannon entropy point is located at the maximum η_t point at the top of the frontier, while the LINMAP point is in the middle of the frontier. The TOPSIS and AHP points are close to the minimum LCOE points, respectively. The Taylor diagram of the decision process is shown in Fig. 17.

Figure 17 shows the scatter distribution of the four decision points in the Taylor diagram. In the figure, the correlation coefficient (C_{coef}), root-mean-squared deviation (R_{rmsd}),

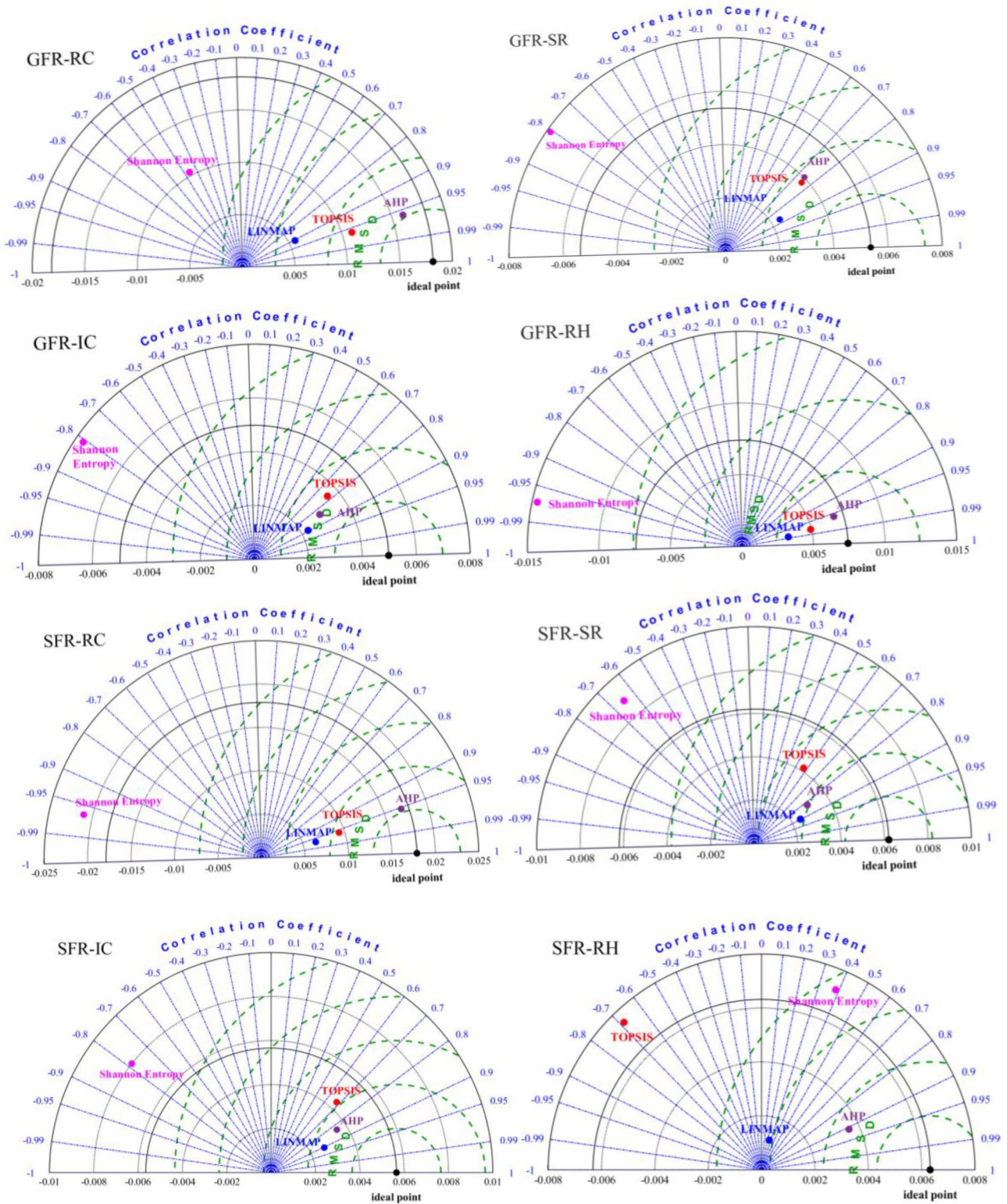


Fig. 17 Taylor diagram for measuring four decision-making points

and standard deviation (S_{std}) are represented by blue dashed lines, green dashed lines, and black arcs, respectively. For example, the C_{coef} , R_{rmsd} , and S_{srd} of the TOPSIS point of

RC in the SFR system are 0.9596, 0.0093, and 0.0094, respectively. The values of the ideal point are 1, 0, and 0.0179, respectively. The ideal point in the Taylor diagram

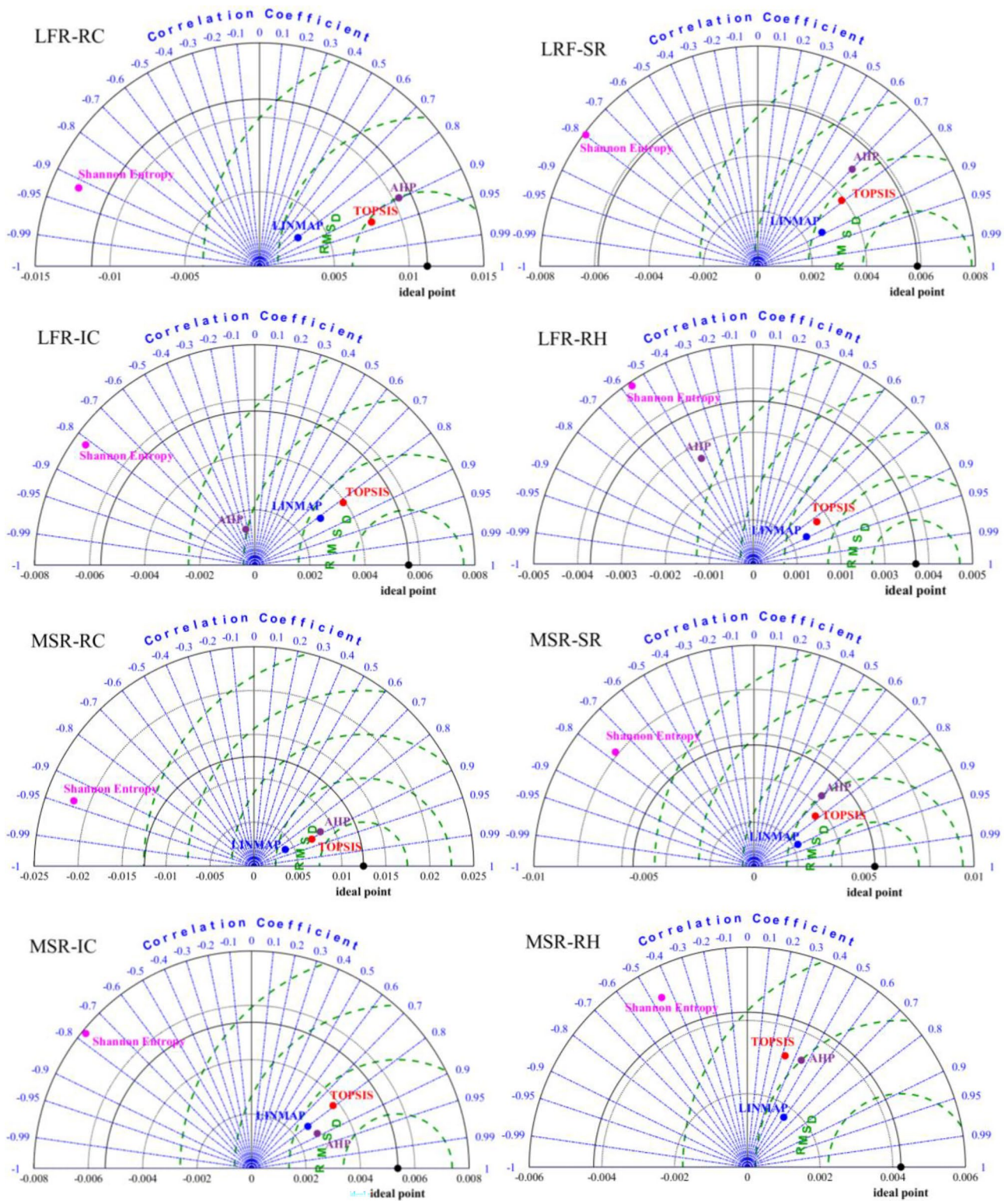


Fig. 17 (continued)

has maximum W_{net} , η_t , η_e , and IRR, and minimum LCOE, C_{tot} , SC, APR, and SP, which differs from the interpretation of the Pareto optimal frontier. These decision points are judged according to the principle that the smaller the R_{rmsd} is, the closer the absolute value of C_{coef} is to 1, and the decision point closer to the ideal point is selected. The Shannon point is noticeably always far away from the ideal point, which indicates that the single-objective optimal result (maximum η_t) should not be chosen as the optimized working condition. From Fig. 17, the R_{rmsd} of ideal, Shannon entropy, LINMAP, TOPSIS and AHP points in the SFR-RC system are 0, 0.0386, 0.0117, 0.0093 and 0.0054, the C_{coef} are 1, -0.9648 , 0.9682, 0.9596 and 0.9529, and the S_{std} are 0.0178, 0.0210, 0.0065, 0.0094, and 0.00170, respectively. Therefore, the AHP is determined as the final optimal Pareto solution closest to the ideal point. Similarly, the R_{rmsd} of the four decision points in the GFR-SR system are 0.01376 and 0.00417, 0.00512 and 0.0041, and the C_{coef} are -0.6512 , 0.8969, 0.5718 and 0.8245. The R_{rmsd} of Shannon entropy and TOPSIS points are larger, and the R_{rmsd} of LINMAP and AHP are close, but the C_{coef} of LINMAP is closer to 1. Therefore, the LINMAP point is chosen as the optimal point. Figure 18 summarizes the specific values in the Taylor diagram for all scenarios.

Table 13 shows the specific values of the multi-objective optimization results. Notably, the shunt ratio (SR) and the primary compression pressure (P_c) are concentrated around 50% and 8.0 MPa, which are the minimum values of their iteration ranges. The smaller cycle shunt ratio improves the narrow point temperature difference of the cycle, increasing the heat transfer efficiency of the cycle, which in turn improves the net cycle efficiency and reduces the power generation cost. Smaller primary compression pressure can reduce the primary compression energy consumption and thus improve the cycle efficiency. The cycle maximum temperature is close to the maximum of their iterations, indicating that within a certain range, the higher the turbine inlet temperature is, the higher the net cycle efficiency is and the lower the LCOE is. The optimal value of the cycle maximum pressure (P_{max}) is around 20 MPa or 30 MPa near the upper limit of the iterative range. A higher pressure does not imply better thermodynamic efficiency of the system and the cost of power generation. RC and RH cycles can achieve better thermodynamic and techno-economic performance with a lower cycle pressure. The η_C and η_T are in the range of 84–89%, which indicates that although the efficiency of the cycle is higher with larger η_C and η_T , the cost of the system also increases. An appropriate value can make the thermodynamic and economic performance of the system reach the optimal value. Most of the final decision points fall under

the AHP, TOPSIS, and LINMAP schemes, and the Shannon entropy method does not apply in the optimization decision.

The specific data for schemes before and after optimization are given in Tables 14 and 15. Figure 19 shows the percentage change of each index before and after optimization. Comparing the data before and after optimization shows that the entire system performance improved significantly after NSGA-II optimization. The positive change indicates an increase, while the negative change represents a decrease. The net output power (W_{net}), net efficiency (η_t), and exergy efficiency (η_e) all show an increasing trend, which indicates that the thermodynamic performance of the system has a great improvement after the optimization of operating parameters. The MSR-IC scheme has the most obvious improvement, with the three indices increasing by 8.58%, 8.58%, and 11.21%, respectively.

The SC and LCOE show a decreasing trend, and the IRR shows an increasing trend, which means that the overall economy of the system is improved. However, the C_{tot} of the system also increases. This is because the η_t and the LCOE as the optimization objectives do not consider the C_{tot} simultaneously, and they are mutually constrained. The LFR-SR scheme has the largest increase in C_{tot} , by 27.78%, while its IRR increases by only 7.8%. This optimization improves the thermodynamic efficiency of the system and the later revenue of the plant, but the optimization results are not friendly to investors with limited funds. For different cycle arrangements, the change in SP is not the same, where the compactness of the turbine for IC and SR has, respectively, improved by 10–15%, while the compactness of RC and RH has decreased, the compactness of SFR-RC has decreased by 3.79%, and the rest is not significant.

4.3 Comprehensive multi-index evaluation results

After processing the indexes of the optimized scheme using the G1 + TOPSIS method, we obtained the strengths and weaknesses of each index at each level for each scheme, as shown in Fig. 20. Each color line in the diagram represents a combination of reactor and cycle arrangement, and the area enclosed by the diagram lines represents the degree of superiority or inferiority of this option. From the figure, the area enclosed by RC is the largest, which indicates that RC has the best overall performance among the four-cycle layouts, followed by SR and IC, and the worst is RH. The C10 index of SR is more prominent, and the C10 index of RC is more depressed, which indicates that the heat transfer area required for RC to obtain unit net output power is larger, and the system is less compact. Although all the indexes of RH are poor, its C6 index is the most prominent among

Fig. 18 C_{coef} , R_{rmsd} , and S_{std} of the Taylor diagram

GFR-RC	Ccoef	Rrmsd	Sstd
Ideal point	1	0	0.01815
Shannon Entropy	-0.46126	0.0247	0.01036
LINMAP	0.90497	0.01329	0.00561
TOPSIS	0.96124	0.00821	0.01094
AHP	0.95946	0.00529	0.01607

GFR-SR	Ccoef	Rrmsd	Sstd
Ideal point	1	0	0.00536
Shannon Entropy	-0.80636	0.0126	0.00787
LINMAP	0.87167	0.00352	0.00233
TOPSIS	0.75507	0.00352	0.00381
AHP	0.74271	0.00359	0.00402

GFR-RH	Ccoef	Rrmsd	Sstd
Ideal point	1	0	0.00741
Shannon Entropy	-0.97124	0.0219	0.01463
LINMAP	0.98521	0.0042	0.0033
TOPSIS	0.97763	0.00278	0.00493
AHP	0.95941	0.00212	0.00674

GFR-IC	Ccoef	Rrmsd	Sstd
Ideal point	1	0	0.00498
Shannon Entropy	-0.808	0.01208	0.0077
LINMAP	0.89345	0.00313	0.00226
TOPSIS	0.77369	0.00317	0.00358
AHP	0.8402	0.00297	0.00294

SFR-RC	Ccoef	Rrmsd	Sstd
Ideal point	1	0	0.01788
Shannon Entropy	-0.96479	0.03858	0.02104
LINMAP	0.96822	0.01171	0.00649
TOPSIS	0.95964	0.00927	0.00937
AHP	0.95292	0.00542	0.01701

SFR-SR	Ccoef	Rrmsd	Sstd
Ideal point	1	0	0.0062
Shannon Entropy	-0.65116	0.01376	0.0089
LINMAP	0.89694	0.00417	0.00241
TOPSIS	0.57176	0.00512	0.00416
AHP	0.82448	0.00408	0.00303

SFR-RH	Ccoef	Rrmsd	Sstd
Ideal point	1	0	0.00632
Shannon Entropy	0.38405	0.00756	0.00723
LINMAP	0.25135	0.00613	0.00114
TOPSIS	-0.68619	0.01272	0.00752
AHP	0.90894	0.00339	0.00361

SFR-IC	Ccoef	Rrmsd	Sstd
Ideal point	1	0	0.00565
Shannon Entropy	-0.78569	0.01293	0.008
LINMAP	0.90371	0.00345	0.00265
TOPSIS	0.67837	0.00419	0.00436
AHP	0.83549	0.00332	0.00355

LFR-RC	Ccoef	Rrmsd	Sstd
Ideal point	1	0	0.01122
Shannon Entropy	-0.91707	0.0239	0.01319
LINMAP	0.80257	0.00886	0.00321
TOPSIS	0.92982	0.00476	0.00806
AHP	0.89692	0.00497	0.01039

LFR-SR	Ccoef	Rrmsd	Sstd
Ideal point	1	0	0.00587
Shannon Entropy	-0.79828	0.01309	0.00792
LINMAP	0.88675	0.00372	0.00266
TOPSIS	0.79049	0.00367	0.0039
AHP	0.70177	0.00426	0.00494

LFR-RH	Ccoef	Rrmsd	Sstd
Ideal point	1	0	0.00371
Shannon Entropy	-0.56245	0.00764	0.00491
LINMAP	0.89114	0.00257	0.00136
TOPSIS	0.83368	0.00245	0.00174
AHP	-0.44066	0.00545	0.00268

LFR-IC	Ccoef	Rrmsd	Sstd
Ideal point	1	0	0.00559
Shannon Entropy	-0.81545	0.01252	0.00754
LINMAP	0.81495	0.00363	0.00293
TOPSIS	0.81696	0.00329	0.00393
AHP	-0.24426	0.00606	0.00134

MSR-RC	Ccoef	Rrmsd	Sstd
Ideal point	1	0	0.01246
Shannon Entropy	-0.94002	0.03378	0.0218
LINMAP	0.88376	0.0091	0.00403
TOPSIS	0.90667	0.00663	0.00726
AHP	0.88784	0.00628	0.00849

MSR-SR	Ccoef	Rrmsd	Sstd
Ideal point	1	0	0.00549
Shannon Entropy	-0.77251	0.01287	0.00815
LINMAP	0.89387	0.00364	0.00223
TOPSIS	0.77411	0.00354	0.0036
AHP	0.69337	0.00401	0.00444

MSR-RH	Ccoef	Rrmsd	Sstd
Ideal point	1	0	0.00423
Shannon Entropy	-0.45376	0.00804	0.00519
LINMAP	0.59332	0.0035	0.00169
TOPSIS	0.3241	0.0044	0.00321
AHP	0.45403	0.004	0.00327

MSR-IC	Ccoef	Rrmsd	Sstd
Ideal point	1	0	0.00538
Shannon Entropy	-0.77547	0.0125	0.00786
LINMAP	0.80172	0.00365	0.00258
TOPSIS	0.79215	0.00332	0.00379
AHP	0.88319	0.00323	0.00274

Table 13 Pareto optimal working conditions and decision solutions

Schemes	P_{max} (MPa)	T_{max} (K)	η_C (%)	η_T (%)	SR (%)	ΔT_{cf} (K)	P_z (MPa)	Solutions
GFR-RC	20.7331	903.1488	84.54	84.98	50.34	–	–	AHP
SFR-RC	18.1709	763.1468	85.19	85.19	50.01	–	–	AHP
LFR-RC	19.8486	826.1500	86.14	87.06	50.11	–	–	TOPSIS
MSR-RC	20.0013	834.1500	85.22	85.76	50.00	–	–	AHP
GFR-SR	29.9826	903.1500	84.49	87.27	–	–	–	TOPSIS
SFR-SR	29.3426	763.1499	85.44	88.03	–	–	–	AHP
LFR-SR	29.9884	826.1500	86.39	88.06	–	–	–	LINMAP
MSR-SR	29.9921	834.1255	85.1	87.43	–	–	–	TOPSIS
GFR-RH	20.1769	903.1485	83.78	86.19	–	7.4083	–	AHP
SFR-RH	18.8858	763.1500	87.19	88.75	–	9.7056	–	LINMAP
LFR-RH	20.6056	826.1500	87.07	87.88	–	9.9534	–	TOPSIS
MSR-RH	20.6007	834.1500	86.75	88.65	–	9.9981	–	LINMAP
GFR-IC	29.9999	903.1497	84.35	87.56	–	–	8.0000	AHP
SFR-IC	29.9960	763.1494	84.25	87.6	–	–	8.0083	AHP
LFR-IC	29.8960	826.1494	84.44	87.08	–	–	8.0060	TOPSIS
MSR-IC	30.0000	834.1500	84.33	87.97	–	–	8.0126	AHP

Table 14 Results for schemes before optimization

Schemes	W_{net} (kW)	η_t (%)	η_e (%)	C_{tot} (10^6 \$)	SC (\$/W)	LCOE (\$/(KW·h))	IRR (%)	APR (m ² /W)	SP
GFR-RC	1135.50	47.40	56.48	1518.84	1738.86	0.014	24	0.513	0.039
SFR-RC	971.80	40.41	51.81	1574.80	2106.66	0.016	19.3	0.522	0.038
LFR-RC	1048.80	43.81	54.05	1546.38	1916.76	0.015	21.5	0.467	0.038
MSR-RC	1052.67	44.21	54.32	1540.87	1902.91	0.015	21.7	0.459	0.039
GFR-SR	953.05	39.78	45.86	1399.38	1908.80	0.014	24.1	0.223	0.040
SFR-SR	817.71	34.00	41.23	1428.22	2270.59	0.016	19.9	0.215	0.038
LFR-SR	880.19	36.76	43.43	1413.58	2087.78	0.015	21.8	0.199	0.039
MSR-SR	883.33	37.09	43.69	1410.29	2075.53	0.015	22	0.196	0.039
GFR-RH	702.84	29.34	34.94	1336.55	2472.11	0.017	18	0.459	0.057
SFR-RH	663.68	27.60	34.39	1384.00	2710.96	0.018	16.1	0.335	0.055
LFR-RH	716.05	29.91	36.22	1370.82	2488.75	0.017	17.8	0.255	0.056
MSR-RH	718.97	30.19	36.44	1367.98	2473.50	0.017	18	0.247	0.056
GFR-IC	957.81	39.98	44.10	1371.33	1861.26	0.013	24.8	0.494	0.040
SFR-IC	833.75	34.67	39.52	1395.37	2175.70	0.015	20.9	0.549	0.038
LFR-IC	890.58	37.20	41.69	1383.15	2019.01	0.014	22.7	0.505	0.039
MSR-IC	893.03	37.50	41.96	1380.29	2009.33	0.014	22.8	0.498	0.039

all cycle arrangements, which indicates that RH requires the lowest initial investment cost. The C8 index for IC is more prominent, indicating that it has the lowest LCOE. Each scheme has different characteristics that decision-makers can choose according to their needs. All indexes were assembled to finally obtain the comprehensive evaluation results for each scheme, as shown in Fig. 21. The results of the weights calculated in this study using the G1 method are B1 (0.3972), B2 (0.2482), B3 (0.2069), B4 (0.1478).

From the evaluation results, the final reactor ranking is MSR > LFR > SFR > GFR, and the ranking for the cycle layouts is RC > SR > IC > RH. For the nuclear Brayton cycle, MSR-RC is the best scheme, followed by MSR-SR and GFR-RC, and the worst evaluation results are GFR-SR and GFR-RH. The results analysis is because safety is considered more important, and MSR has the best safety. The results of the cycle layouts ranking are consistent with the previous single-objective analysis.

Table 15 Results for schemes after optimization

Schemes	W_{net} (kW)	η_t (%)	η_e (%)	C_{tot} (10 ⁶ \$)	SC (\$/W)	LCOE (\$/(KW·h))	IRR (%)	APR (m ² /W)	SP
GFR-RC	1208.81	50.46	62.81	1797.04	1486.62	0.012	28.5	0.263	0.040
SFR-RC	1012.70	42.11	56.71	1840.04	1816.96	0.014	22.9	0.196	0.039
LFR-RC	1138.21	47.54	60.59	1905.22	1673.88	0.014	25	0.277	0.039
MSR-RC	1123.27	47.17	60.56	1841.93	1639.79	0.013	25.6	0.290	0.039
GFR-SR	990.18	41.33	49.08	1727.39	1744.53	0.013	26.6	0.153	0.035
SFR-SR	846.09	35.18	44.31	1801.34	2129.00	0.015	21.4	0.156	0.034
LFR-SR	922.60	38.53	46.85	1806.26	1957.79	0.014	23.5	0.140	0.035
MSR-SR	916.01	38.47	46.89	1753.89	1914.71	0.014	24.1	0.140	0.035
GFR-RH	757.27	31.61	37.73	1619.85	2139.06	0.015	21.3	0.279	0.057
SFR-RH	666.85	27.73	34.59	1734.03	2600.31	0.018	16.9	0.227	0.055
LFR-RH	718.78	30.02	36.31	1694.69	2357.73	0.016	19	0.254	0.056
MSR-RH	726.96	30.53	36.73	1714.08	2357.88	0.016	19	0.242	0.056
GFR-IC	1038.81	43.36	48.81	1713.79	1649.76	0.012	28.3	0.337	0.036
SFR-IC	897.88	37.33	43.94	1744.44	1942.84	0.014	23.7	0.389	0.034
LFR-IC	959.08	40.06	46.10	1713.28	1786.38	0.013	25.9	0.356	0.035
MSR-IC	969.69	40.72	46.66	1740.60	1795.00	0.013	25.8	0.346	0.035

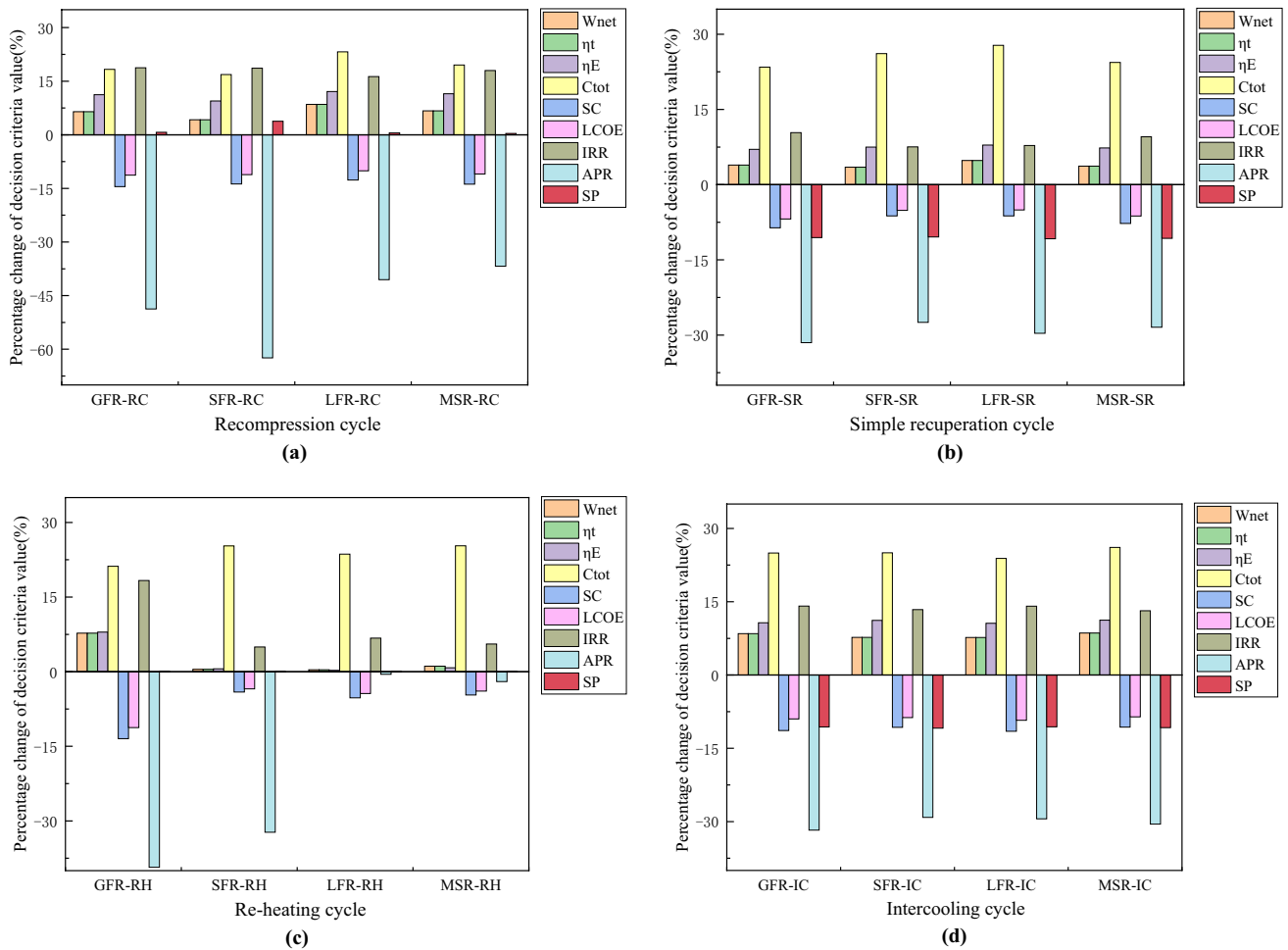


Fig. 19 Percentage change of each index before and after optimization

Fig. 20 (Color online) Comparison of all indexes of each optimal scheme

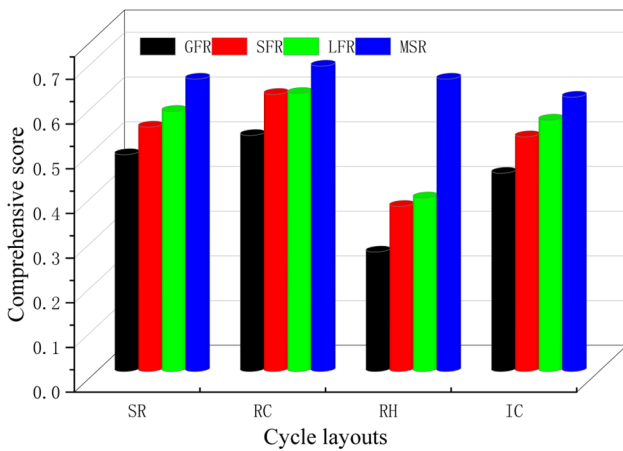
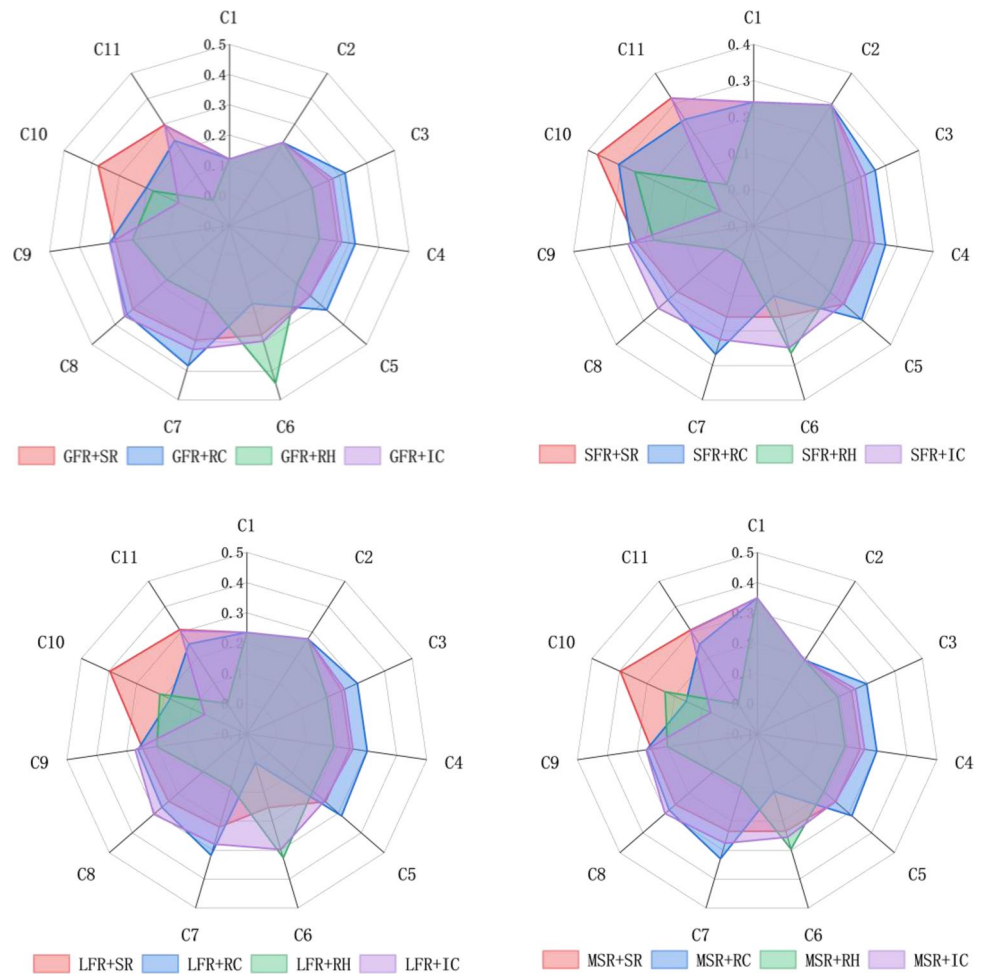


Fig. 21 (Color online) Comprehensive evaluation results

5 Conclusion

In this study, a mathematical model of the Brayton cycle was developed for four different cycle layouts. Parametric analysis was conducted to investigate seven crucial

parameters that affect the thermo-economic performance of the Brayton cycle. The NSGA-II method was used to simultaneously optimize maximizing η_t and minimizing LCOE. Four decision methods obtained the compromise scheme from the Pareto optimal frontiers. Taylor diagrams are used to evaluate the four compromise solutions to find the optimal scheme. The changes in the indexes of each scheme before and after optimization are analyzed and discussed. Finally, the characteristics of each index after optimization for all schemes are given. The main conclusions are summarized as follows:

- (1) Higher pressure does not lead to better thermodynamic efficiency of the system and power generation costs. RC and RH cycles can achieve better thermodynamic and techno-economic performance with a lower cycle pressure.
- (2) The overall performance of the nuclear Brayton cycle system has been improved due to optimization. The MSR-IC scheme has the most noticeable improvement, with the net output power W_{net} , thermodynamic effi-

ciency η_t , and exergy efficiency η_e improved by 8.58%, 8.58%, and 11.21%, respectively.

- (3) The LFR-SR scheme was optimized to increase C_{tot} by 27.78%, while the internal rate of return (IRR) increased by only 7.8%. This is not friendly to investors with limited funds.
- (4) Among the four layouts, RC has the best overall performance, followed by SR and IC, and the worst is RH. However, RH has the lowest C_{tot} , and IC has the lowest LCOE.
- (5) Considering all indices of the four levels, the final reactor ranking is MSR > LFR > SFR > GFR, and the cycle layouts ranking is RC > SR > IC > RH. For the nuclear Brayton cycle, MSR-RC should be given priority, while GFR-RH should be considered carefully.

Supercritical fluid power cycles have great potential for application. In this study, the application of the supercritical CO₂ Brayton cycle in nuclear power plants is considered. The constructed mathematical models and optimization decision methods can guide the design of nuclear power plants and wider energy fields with potential heat resources.

Appendix: Nusselt number and friction factor calculation

For the semi-circular straight channel PCHE, the Nusselt number is calculated by the Gnielinski correlation [44]. The Nusselt number in Eq. (13) is calculated by Eqs. (A1)–(A3).

$$Nu = 4.089 \quad (Re < 2300) \quad (A1)$$

$$Nu = 4.089 + \frac{Nu_{Re=5000} - 4.089}{5000 - 2300} (Re - 2300) \quad (2300 \leq Re < 5000) \quad (A2)$$

$$Nu = \frac{(f_d/8)(Re - 1000)Pr}{1 + 12.7(Pr^{2/3} - 1)\sqrt{f_d/8}} \quad (Re \geq 5000) \quad (A3)$$

$$f_d = \left(\frac{1}{1.8 \log_{10}(Re) - 1.5} \right)^2 \quad (A4)$$

The friction factor (f) used for the Darcy–Weisbach equation [Eq. (16)] depends on the relative roughness of the channels [Eq. (A5)] and the Reynolds number. The Reynolds number from laminar to turbulent flow is calculated by Eqs. (A6)–(A9).

$$\delta = \frac{\epsilon}{d} \quad (A5)$$

$$Re_0 = \begin{cases} 2000, & \delta < 0.007 \\ 754 \exp(0.0065/\delta), & \delta \geq 0.007 \end{cases} \quad (A6)$$

$$Re_1 = \begin{cases} 2000, & \delta < 0.007 \\ 1160(1/\delta)^{0.11}, & \delta \geq 0.007 \end{cases} \quad (A7)$$

$$Re_2 = 2090(1/\delta)^{0.0635} \quad (A8)$$

$$Re_3 = 441.19\delta^{-1.1772} \quad (A9)$$

The friction factor (f) in Eq. (16) is calculated by Eq. (35) [45].

$$f = \frac{64}{Re} \quad (Re < Re_0) \quad (A10)$$

$$f = \begin{cases} 0.032 + 3.895 \times 10^{-7}(Re - 2000), & \delta_{rel} < 0.007 \\ 4.4Re^{-0.595} \exp(-0.00275/\delta_{rel}), & \delta_{rel} \geq 0.007 \end{cases} \quad (Re_0 < Re < Re_1) \quad (A11)$$

When $Re_1 > Re > Re_2$, the f is obtained from Eq. (A12), where f_1 is obtained from the formula given by Idelchik [46], as shown in Eq. (A13). The Colebrook–White correlation [44] is used to calculate f_i , and f_n is calculated by iteration. When the error between f_i and f_n is less than 0.01, it can be assumed that $f_i = f_n$. Eqs. (A16)–(A19) use the same calculation method.

$$f = (f_2 - f_1) \exp \left\{ -[0.0017(Re_2 - Re)]^2 \right\} + f_1 \quad (A12)$$

$$f_1 = \begin{cases} 0.032, & \delta < 0.007 \\ 0.075 - \left(\frac{0.0109}{\delta^{0.286}} \right), & \delta \geq 0.007 \end{cases} \quad (A13)$$

$$f_i = 0.11(\delta + 68/Re_2)^{0.25} \quad (A14)$$

$$f_n = \left[\frac{1}{2 \log_{10} \left(\frac{2.51}{Re_2 \sqrt{f_i}} + \frac{\delta}{3.7} \right)} \right]^2 \quad (A15)$$

When $Re_2 < Re < Re_3$

$$f_i = 0.11(\delta + 68/Re_2)^{0.25} \quad (A16)$$

$$f_n = \left[\frac{1}{2 \log_{10} \left(\frac{2.51}{Re \sqrt{f_i}} + \frac{\delta}{3.7} \right)} \right]^2 \quad (\text{A17})$$

When $Re > Re_3$

$$f_i = 0.11 (\delta + 68/Re_3)^{0.25} \quad (\text{A18})$$

$$f_n = \left[\frac{1}{2 \log_{10} \left(\frac{2.51}{Re_3 \sqrt{f_i}} + \frac{\delta}{3.7} \right)} \right]^2 \quad (\text{A19})$$

For more information on the above equations, it is recommended to refer to the references cited in Appendix.

Author contributions All authors contributed to the study conception and design. Material preparation, data collection, and analysis were performed by G-PY, Y-FC, NZ, and P-JM. The first draft of the manuscript was written by G-PY and Y-FC and supervised by P-JM, and all authors commented on previous versions of the manuscript. All authors read and approved the final manuscript.

Data availability The data that support the findings of this study are openly available in Science Data Bank at <https://cstr.cn/31253.11.sciencedb.13640> and <https://www.doi.org/https://doi.org/10.57760/sciencedb.13640>.

Conflict of interest The authors declare that they have no competing interests.

References

1. N. Bauer, I. Mouratiadou, G. Luderer et al., Global fossil energy markets and climate change mitigation—an analysis with REMIND. *Clim. Change* **136**, 69–82 (2016). <https://doi.org/10.1007/s10584-013-0901-6>
2. J. Koomey, N.E. Hultman, A reactor-level analysis of busbar costs for US nuclear plants, 1970–2005. *Energy Policy* **35**, 5630–5642 (2007). <https://doi.org/10.1016/j.enpol.2007.06.005>
3. S. Nagataki, N. Takamura, A review of the Fukushima nuclear reactor accident: radiation effects on the thyroid and strategies for prevention. *Curr. Opin. Endocrinol. Diabetes Obes.* **21**, 384–393 (2014). <https://doi.org/10.1097/MED.0000000000000098>
4. F. Bertrand, N. Marie, A. Bachrata et al., Simplified criteria for a comparison of the accidental behaviour of Gen IV nuclear reactors and of PWRs. *Nucl. Eng. Des.* **372**, 110962 (2021). <https://doi.org/10.1016/j.nucengdes.2020.110962>
5. P. Hejzlar, N.E. Todreas, E. Shwageraus et al., Cross-comparison of fast reactor concepts with various coolants. *Nucl. Eng. Des.* **239**, 267–291 (2009). <https://doi.org/10.1016/j.nucengdes.2009.07.007>
6. J.E. Kelly, Generation IV international forum: a decade of progress through international cooperation. *Prog. Nucl. Energy* **77**, 240–246 (2014). <https://doi.org/10.1016/j.pnucene.2014.02.010>
7. Y. Ahn, S.J. Bae, M. Kim et al., Review of supercritical CO₂ power cycle technology and current status of research and development. *Nucl. Eng. Technol.* **47**, 647–661 (2015). <https://doi.org/10.1016/j.net.2015.06.009>
8. H. Tian, Z. Xu, P. Liu et al., How to select regenerative configurations of CO₂ transcritical Rankine cycle based on the temperature matching analysis. *Int. J. Hydrog. Energy* **44**, 2560–2579 (2020). <https://doi.org/10.1002/er.4945>
9. R.V. Padilla, R. Benito, W. Stein, An exergy analysis of recompression supercritical CO₂ cycles with and without reheating. *Energy Procedia* **69**, 1181–1191 (2015). <https://doi.org/10.1016/j.egypro.2015.03.201>
10. I. Pioro. *Handbook of Generation-IV Nuclear Reactors* (American Society of Mechanical Engineers Digital Collection, 2017). <https://doi.org/10.1016/C2014-0-01699-1>
11. H. Li, Y. Zhang, M. Yao et al., Design assessment of a 5 MW fossil-fired supercritical CO₂ power cycle pilot loop. *Energy* **174**, 792–804 (2019). <https://doi.org/10.1016/j.energy.2019.02.178>
12. B.S. Oh, Y.H. Ahn, H. Yu et al., Safety evaluation of supercritical CO₂ cooled micro modular reactor. *Ann. Nucl. Energy* **110**, 1202–1216 (2017). <https://doi.org/10.1016/j.energy.2019.02.178>
13. J.H. Park, H.S. Park, J.G. Kwon et al., Optimization and thermodynamic analysis of supercritical CO₂ Brayton recompression cycle for various small modular reactors. *Energy* **160**, 520–535 (2018). <https://doi.org/10.1016/j.energy.2018.06.155>
14. Y.-N. Ma, P. Hu, C.-Q. Jia et al., Thermo-economic analysis and multi-objective optimization of supercritical Brayton cycles with CO₂-based mixtures. *Appl. Therm. Eng.* **219**, 119492 (2023). <https://doi.org/10.1016/j.applthermaleng.2022.119492>
15. S.J. Bae, Y. Ahn, J. Lee, et al., Hybrid system of Supercritical Carbon Dioxide Brayton cycle and carbon dioxide rankine cycle combined fuel cell, in *Turbo Expo: Power for Land, Sea, and Air*, vol. 45660 (American Society of Mechanical Engineers, 2014), p. V03BT36A004
16. K. Wang, Y.-L. He, H.-H. Zhu, Integration between supercritical CO₂ Brayton cycles and molten salt solar power towers: a review and a comprehensive comparison of different cycle layouts. *Appl. Energy* **195**, 819–836 (2017). <https://doi.org/10.1016/j.apenergy.2017.03.099>
17. L. Shi, H. Tian, G. Shu, Multi-mode analysis of a CO₂-based combined refrigeration and power cycle for engine waste heat recovery. *Appl. Energy* **264**, 114670 (2020). <https://doi.org/10.1016/j.apenergy.2020.114670>
18. S. Kim, Y. Cho, M.S. Kim et al., Characteristics and optimization of supercritical CO₂ recompression power cycle and the influence of pinch point temperature difference of recuperators. *Energy* **147**, 1216–1226 (2018). <https://doi.org/10.1016/j.energy.2017.12.161>
19. J. Song, X.-S. Li, X.-D. Ren et al., Performance analysis and parametric optimization of supercritical carbon dioxide (S-CO₂) cycle with bottoming organic Rankine cycle (ORC). *Energy* **143**, 406–416 (2018). <https://doi.org/10.1016/j.energy.2017.10.136>
20. X. Bian, X. Wang, R. Wang et al., A comprehensive evaluation of the effect of different control valves on the dynamic performance of a recompression supercritical CO₂ Brayton cycle. *Energy* **248**, 123630 (2022). <https://doi.org/10.1016/j.energy.2022.123630>
21. R. Wang, X. Li, Z. Qin et al., Dynamic response and emergency measures under failure conditions of sCO₂ Brayton cycle. *Energy Sci. Eng.* **10**, 4726–4746 (2022). <https://doi.org/10.1002/ese3.1300>
22. K. Wang, M.-J. Li, J.-Q. Guo et al., A systematic comparison of different S-CO₂ Brayton cycle layouts based on multi-objective optimization for applications in solar power tower plants. *Appl. Energy* **212**, 109–121 (2018). <https://doi.org/10.1016/j.apenergy.2017.12.031>
23. F.G. Battisti, J.M. Cardemil, A.K. da Silva, A multivariable optimization of a Brayton power cycle operating with CO₂ as working fluid. *Energy* **112**, 908–916 (2016). <https://doi.org/10.1016/j.energy.2016.06.118>

24. J. Wang, Z. Sun, Y. Dai, S. Ma, Parametric optimization design for supercritical CO₂ power cycle using genetic algorithm and artificial neural network. *Appl. Energy* **87**, 1317–1324 (2010). <https://doi.org/10.1016/j.apenergy.2009.07.017>
25. M.M. Naserian, S. Farahat, F. Sarhaddi, Exergoeconomic multi objective optimization and sensitivity analysis of a regenerative Brayton cycle. *Energy Convers. Manag.* **117**, 95–105 (2016). <https://doi.org/10.1016/j.enconman.2016.03.014>
26. Y. Li, G. Liu, X. Liu et al., Thermodynamic multi-objective optimization of a solar-dish Brayton system based on maximum power output, thermal efficiency and ecological performance. *Renew. Energ.* **95**, 465–473 (2016). <https://doi.org/10.1016/j.renene.2016.04.052>
27. O.L. De Weck, Multiobjective optimization: history and promise, in *The Third China-Japan-Korea Joint Symposium on Optimization of Structural and Mechanical Systems* (Kanazawa, Japan, 2004)
28. Z. Hu, D. He, H. Zhao, Multi-objective optimization of energy distribution in steel enterprises considering both exergy efficiency and energy cost. *Energy* **263**, 125623 (2023). <https://doi.org/10.1016/j.energy.2022.125623>
29. Y. Li, S. Liao, G. Liu, Thermo-economic multi-objective optimization for a solar-dish Brayton system using NSGA-II and decision making. *Int. J. Elec. Power.* **64**, 167–175 (2015). <https://doi.org/10.1016/j.ijepes.2014.07.027>
30. R. Kumar, S. Kaushik, R. Kumar et al., Multi-objective thermodynamic optimization of an irreversible regenerative Brayton cycle using evolutionary algorithm and decision making. *Ain. Shams. Eng. J.* **7**, 741–753 (2016). <https://doi.org/10.1016/j.asej.2015.06.007>
31. R.V. Rao, H.S. Keesari, Rao algorithms for multi-objective optimization of selected thermodynamic cycles. *Eng. Comput.* **37**, 3409–3437 (2021). <https://doi.org/10.1007/s00366-020-01008-9>
32. V. Dostal, M.J. Driscoll, P. Hejzlar, *A Supercritical Carbon Dioxide Cycle for Next Generation Nuclear Reactors* (MIT-ANP-TR-100, Cambridge, 2004). <https://doi.org/10.13182/NT154-265v>
33. Y. Chang, P. Finck, C. Grandy et al., *Advanced Burner Test Reactor Preconceptual Design Report* (Argonne National Lab, Lemont, 2008)
34. K. Schultz, L. Brown, G. Besenbruch et al., *Large-Scale Production of Hydrogen by Nuclear Energy for the Hydrogen Economy* (General Atomics, San Diego, 2003)
35. A. Bejan, G. Tsatsaronis, M.J. Moran, *Thermal Design and Optimization* (Wiley, New York, 1995). [https://doi.org/10.1016/s0360-5442\(96\)90000-6](https://doi.org/10.1016/s0360-5442(96)90000-6)
36. M. Marchionni, G. Bianchi, S.A. Tassou, Techno-economic assessment of Joule–Brayton cycle architectures for heat to power conversion from high-grade heat sources using CO₂ in the supercritical state. *Energy* **148**, 1140–1152 (2018). <https://doi.org/10.1016/j.energy.2018.02.005>
37. Y. Cao, H.N. Rad, D.H. Jamali et al., A novel multi-objective spiral optimization algorithm for an innovative solar/biomass-based multi-generation energy system: 3E analyses, and optimization algorithms comparison. *Energy. Convers. Manag.* **219**, 112961 (2020). <https://doi.org/10.1016/j.enconman.2020.112961>
38. X. Wang, Y. Guo, Consistency analysis of judgment matrix based on G1 method. *Chin. J. Manag. Sci.* **14**, 65–70 (2012). <https://doi.org/10.3321/j.issn:1003-207X.2006.03.012>
39. K. Tuček, J. Carlsson, H. Wider, Comparison of sodium and lead-cooled fast reactors regarding reactor physics aspects, severe safety and economical issues. *Nucl. Eng. Des.* **236**, 1589–1598 (2006). <https://doi.org/10.1016/j.nucengdes.2006.04.019>
40. C. Handwerk, M. Driscoll, P. Hejzlar, *Use of Beryllium Oxide to Shape Power and Reduce Void Reactivity in Gas-Cooled Fast Reactors*, ANS Topical Meeting on Reactor Physics (Vancouver, Canada, 2006)
41. E. Hoffman, W. Yang, R. Hill, *Preliminary Core Design Studies for the Advanced Burner Reactor Over a Wide Range of Conversion Ratios* (Argonne National Lab, Lemont, 2008)
42. A. Nikiforova, P. Hejzlar, N.E. Todreas, Lead-cooled flexible conversion ratio fast reactor. *Nucl. Eng. Des.* **239**, 2596–2611 (2009). <https://doi.org/10.1016/j.nucengdes.2009.07.013>
43. S. Mondal, S. De, CO₂ based power cycle with multi-stage compression and intercooling for low temperature waste heat recovery. *Energy* **90**, 1132–1143 (2015). <https://doi.org/10.1016/j.energy.2015.06.060>
44. W.C. Williams, P. Hejzlar, P. Saha, Analysis of a convection loop for GFR post-LOCA decay heat removal. *Nucl. Sci. Eng.* **1**, 753–762 (2004). <https://doi.org/10.1115/icon12-49360>
45. H. Li, Y. Yang, Z. Cheng et al., Study on off-design performance of transcritical CO₂ power cycle for the utilization of geothermal energy. *Geothermics* **71**, 369–379 (2018). <https://doi.org/10.1016/j.geothermics.2017.09.002>
46. I.E. Idelchik, *Handbook of Hydraulic Resistance* (Washington, Seattle, 1986)

Springer Nature or its licensor (e.g. a society or other partner) holds exclusive rights to this article under a publishing agreement with the author(s) or other rightsholder(s); author self-archiving of the accepted manuscript version of this article is solely governed by the terms of such publishing agreement and applicable law.